

g-C₃N₄/Ti₃C₂T_x(MXenes) Composite with Oxidized Surface Groups for Efficient Photocatalytic Hydrogen Evolution

Yuliang Sun^a, Di Jin^a, Yuan Sun^a, Xing Meng^{a,c,*}, Yu Gao^a, Yohan Dall'Agnesse^a, Gang Chen^{a,b}, Xiao-Feng Wang^{a,*}

^a*Key Laboratory of Physics and Technology for Advanced Batteries (Ministry of Education), College of Physics, Jilin University, Changchun 130012, PR China*

^b*State Key Laboratory of Superhard Materials, Jilin University, Changchun 130012, PR China*

^c*A. J. Drexel Nanomaterials Institute, and Department of Materials Science and Engineering, Drexel University, Philadelphia, Pennsylvania 19104, United States*

*Xiao-Feng Wang E-mail: xf_wang@jlu.edu.cn

*Xing Meng E-mail: mengxing@jlu.edu.cn

Abstract

Ti₃C₂T_x is a 2-dimensional titanium carbide material featuring outstanding electrochemical properties. In spite of this, application of Ti₃C₂T_x as co-catalyst in photo-catalysis is rarely under explored probably because of its metallic nature and the hydrophilic surface. Given that

$Ti_3C_2T_x$ with different surface terminations exhibits large differences in catalytic, electrochemical and chemical properties, we demonstrate improvement of the photocatalytic activity of $Ti_3C_2T_x$ as a co-catalyst by annealing a composite of carbon nitride and $Ti_3C_2T_x$. $Ti_3C_2T_x$ with the oxygen terminated surface improves the separation of electron-hole pairs resulting in 105% enhancement in production ratio in hydrogen evolution as compared with the control samples. The best hydrogen production performance achieves as high as 88 $\mu\text{mol/h/g.cat}$. The apparent quantum yield (AQY) achieves as high as 1.27%. The DFT calculations also demonstrate a better hydrogen evolution on Ti_3C_2 with oxygen surface termination.

Key words: MXenes, photocatalysis, surface termination groups, hydrogen evolution, DFT calculation.

Introduction

The traditional energy sources such as coal, oil and natural gas are unsustainable and will leave an energy gap of 14TW by the year of 2050. To fill that energy gap, solar energy is considered the only available renewable energy resource with such a potential. Photocatalytic hydrogen evolution from water is an effective way to convert solar energy into chemical energy that is much easy to store. Semiconductor-based photocatalysts can split water into hydrogen and oxygen under the presence of co-catalysts, which are normally noble metals such as Pt, Ru, Rh, Pd. Among the semiconductors being developed nowadays, 2-dimensional (2D) photocatalyst g- C_3N_4 is promising because of its merits such as high stability, large surface area, non-toxicity and suitable band gap.¹⁻³ To improve the

photocatalytic activity of $g\text{-C}_3\text{N}_4$, various means are reported, including nanoarchitecture design, elemental doping, copolymerization and heterojunction nanostructures design.⁴ The noble-metal-free photocatalytic hydrogen evolution is also investigated such as metal chalcogenide, metal phosphide, metal oxide or even graphene to replace the high cost noble metal cocatalyst.⁵⁻⁹ Zeng et al achieves 535.7 $\mu\text{mol/g/h}$ with Ni_{12}P_5 as cocatalyst⁶ and 474.7 $\mu\text{mol/g/h}$ with Ni_2P .⁹

MXenes are a new family of 2D nanostructure materials, initially reported in 2011.¹⁰ MXenes are prepared from MAX phase by etching the A-layer (usually Al) with strong acid solutions such as HF or LiF/HCl. MXenes have a general formula of $\text{M}_{n+1}\text{X}_n\text{T}_x$ ($n = 1-3$), in which M represents an early transition metal, e.g., Ti, V, Nb, Ta, Mo, X is carbon and/or nitrogen, and T_x stands for the surface termination groups such as -O, -F and -OH.^{11, 12} MXenes have been applied to different fields including energy storage,¹³⁻²⁰ electromagnetic interference shielding,²¹⁻²³ water purification and catalysis for the electronic.²⁴⁻²⁷

The photo- and electro-catalytic properties of MXenes were predicted by the density functional theory(DFT) calculations.^{28, 29} Moreover, Mo_2CT_x and Ti_2CT_x were already investigated in electro-catalytic hydrogen evolution reaction (HER).²⁷ Mo_2CT_x exhibits good performance in stability, hydrogen evolution activity, and lower over potential. Nanocomposites of semiconductors and MXene, e.g., $\text{TiO}_2/\text{Ti}_3\text{C}_2$ were hydro-thermally synthesized to study their catalytic activity.³⁰ As a result, methyl orange(MO) is photocatalytic degraded in the presence of such composites when NaBF_4 is used to control the morphology of the composite.³¹ $\text{TiO}_2/\text{Ti}_3\text{C}_2\text{T}_x$, $\text{TiO}_2/\text{Ti}_2\text{CT}_x$ and $\text{TiO}_2/\text{Nb}_2\text{CT}_x$ composites have been tested as photo-catalysts for hydrogen production. Among these, $\text{TiO}_2/\text{Nb}_2\text{CT}_x$

exhibits the best performance.³² Besides, CdS/Ti₃C₂T_x was also synthesized by hydrothermal method, and Ti₃C₂T_x with small diameter but large surface area gives an excellent performance as the co-catalyst in photocatalytic HER.³³ Ti₂C is also found to exhibit co-catalysis in combination with the catalyst of g-C₃N₄ for HER.³⁴ Moreover, in situ oxidation of MXenes is also proved photocatalytic^{30, 35} and CO₂ conversion can also be achieved with the cocatalysis of MXenes.^{36, 37}

Surface terminations greatly affect the physicochemical properties of MXenes. Bare MXenes without termination groups have not been synthesized yet. Different synthetic methods produce different surface termination groups on MXenes. For example, MXenes etched by HF contain mainly -F terminations whereas those etched by LiF/HCl contain more -O terminations.³⁸ Post-treatment on as-prepared MXenes, however, alters the composition of the surface terminations, e.g., the -F terminations can be replaced gradually by -O terminations in the air.³⁹ In view of this, MXenes with -F terminations are much unstable compared with that with other terminations. -OH terminations transform into -O terminations at 200°C as depicted by the following equation:⁴⁰



The DFT calculations suggest that -O terminations may give better Li-ion storage capacity or behave as the HER active sites.^{16, 33, 39} In fact, the free energy of Ti₃C₂ with -O terminations is much lower than that of Pt and thus Ti₃C₂ with -O terminations may become an efficient and low-cost alternative of Pt in HER.³³ The composition of surface termination groups is not controllable in synthesis, but is controllable with hydrothermal or thermal

treatment. The presence of O₂ alters the surface termination groups efficiently by oxidizing Ti into TiO₂ at a high annealing temperature.⁴¹

Herein, we hybridized the composite of g-C₃N₄/Ti₃C₂T_x by a scalable process and tuned the surface chemistry of Ti₃C₂T_x by post-annealing in both air and N₂ atmospheres. **The composite is very easily hybridized by the mixing in a mortar without other process such as hydrothermal, which was really a fast way.** The prepared Ti₃C₂T_x is employed as co-catalyst with g-C₃N₄ photocatalyst for the HER. The -O surface terminations clearly enhance the amount of hydrogen produced at the active sites. This research paves a way to replace the high-cost and precious metal co-catalysts in HER and to accelerate the development of HER for renewable energy revolution. The DFT calculations are also done to demonstrate the HER activity for different surface termination groups.

Experimental section

2.1 The synthesis of g-C₃N₄ and Ti₃C₂ MXenes

For the synthesis of g-C₃N₄, NH₄Cl is used as a template. Briefly, 2 g of dicyandiamide powder and 10 g ammonium chloride are dissolved in 100 ml deionized water and stirred at 75°C until the mixture is separated out. The mixture is then heated in a muffle furnace at 550°C for 4 h, and at a rate of 5°C/min.⁴² A mortar is used to make the bulky g-C₃N₄ into powder.

Ti₃C₂T_x MXenes is obtained from etching Ti₃AlC₂ (Forsman, 98%) in 49% HF. 1 g Ti₃AlC₂ is added into 10 ml 49% HF slowly with stirring at a rate of 200 rpm at room temperature for 24 h. The etched suspension is then washed by deionized water and

centrifuged until the pH value near 7. The black wet powder is dried in a vacuum oven at 60°C overnight.

2.2 The preparation of g-C₃N₄/Ti₃C₂T_x composites

The yellow g-C₃N₄ powder and the black Ti₃C₂T_x powder are mixed with a pestle and mortar at different ratios. To modify the Ti₃C₂ surface terminations, the mixtures are then annealed for one hour at 200°C either in a tube furnace under N₂ protection or in a muffle oven in air. The samples with a mass ratio of Ti₃C₂T_x and g-C₃N₄ controlled at 3 : 10 were selected for further characterization and labelled 30%.

2.3 Characterizations

To characterize the g-C₃N₄, Ti₃C₂ and the composites powders, the X-ray diffractometer (XRD, DX-2700B) is operated at 40 KV and 200mA with Cu K α radiation($\lambda = 0.15406$ nm). Scanning electron microscopy (SEM, JSM-6700F) is used to observe the morphology of the samples. X-ray photoelectron spectroscopy (XPS, ESCALAB) analysis is conducted using a Mg-K α light source to confirm the element ratio of the samples. Specific surface area measurements (Kubo-X1000) are typically based on N₂ sorption with pretreatment at 60°C under the Brunauer-Emmer-Teller (BET) model. Photoluminescence emission spectra (PL) are determined using a fluorescence spectrometer (Shimadzu RF-5301) at the 340 nm excitation and the powder samples are tested directly. Fourier Transform infrared spectroscopy (FTIR, Vertex 70, Bruker, Germany) is used in a range of 400 to 4000 cm⁻¹ to record the spectra for samples. Ultraviolet-Visible diffuse reflectance spectra (UV-Vis DRS, Specord 210 plus, Analytikjena, Germany) are measured for the absorption of samples under UV-Vis light with an optics integrating sphere using BaSO₄ as the standard. **High resolution**

transmission electron microscopy (HRTEM, FEI Tecnai G2 F20) is used to observe the heterojunction interface between g-C₃N₄ and Ti₃C₂T_x.

2.4 Photocatalytic activity measurements

Photocatalytic H₂ evolution is measured under a 350 W xenon lamp (AHD 350, ShenzhenAnhongda Opto Technology Co. Ltd., China). A 6 ml photoreactor and a cut-off filter ($\lambda > 400$ nm) are used. Photocatalyst powder in which g-C₃N₄ is controlled at 3 mg for the same condition is dispersed in 3 mL aqueous solution with 10 vol% triethanolamine as the hole sacrificial reagent and a magnetic bar to prevent the sedimentation of the photocatalysts during the 6 h measurement. O₂ is removed by the purging of Ar gas before the photocatalytic activity measurements. H₂ evolution is tested by a gas chromatography (SP-3420A, Beifen-Ruili, China) with Ar as carrier gas. H₂ evolution for Pt as cocatalyst was also test in the system. 1%, 2%, 3%, 4% and 5% Pt (H₂PtCl₆, mass ratio to g-C₃N₄) were used. The apparent quantum yield (AQY) which assesses the efficiency of photons conversion is calculated as following^{6,9}:

$$\begin{aligned} \text{AQY}(\%) &= \frac{\text{the number of reacted electrons}}{\text{the number of incident photons}} \times 100\% \\ &= \frac{\text{the number of evolved } H_2 \text{ molecules} \times 2}{\text{the number of incident photons}} \times 100\% \end{aligned}$$

2.5 DFT calculation method

Vienna ab initio simulation package (VASP)^{43, 44} was used in the DFT calculations. Generalized gradient approximation (GGA) in the Perdew - Burke - Ernzerhof (PBE)^{45, 46} form was used in the calculations. A plane wave cutoff energy of 600 eV is sufficient to ensure the convergence of total energies to 1 meV per primitive cell. Supercells were

consisted of $2 \times 2 \times 1$ unit cells and the Brillouin zone was sampled using Monkhorst - Pack mesh $6 \times 6 \times 1$ for them. The forces were converged to $0.01 \text{ eV}/\text{\AA}$ or below for all structures and the energy accuracy was set at 10^{-6} eV . Van der Waals forces were considered. The vacuum space at least 30 \AA was used to avoid the interaction. Because the increase of hydrogen coverage would lead to the decrease of active sites, 25% and 50% monolayer atomic H coverage was considered.

Results and Discussion

3.1 Characterization of structures and morphology

Fig.1A shows the X-ray diffraction (XRD) patterns of raw and composites materials studied herein. The $\text{Ti}_3\text{C}_2\text{T}_x$ is prepared by etching the Al layer of Ti_3AlC_2 powder with HF. -OH, -F and -O surface termination groups spontaneously generate on the surface of Ti_3C_2 during the HF etching process resulting in enhanced hydrophilicity of Ti_3C_2 .^{33, 38} The XRD shifts of the (002) and (004) peaks to lower degrees together with the disappearance of the strongest peak of Ti_3AlC_2 at 39° are the signs of the removal of Al from MAX phase Ti_3AlC_2 .^{10, 40} The XRD pattern of g- C_3N_4 shows a pair of typical peaks with high intensity at $2\theta = 27.5^\circ$ and with low intensity at $2\theta = 13.1^\circ$, as reported previously.³⁴ The XRD patterns of composites samples suggest that the combination of g- C_3N_4 and Ti_3C_2 is through physical contact. No new XRD peak is generated after mixing them in a pestle and mortar and/or followed by annealing in air or N_2 . These strong peaks at $2\theta = 27.5^\circ$ from g- C_3N_4 and at $2\theta = 9^\circ$ from Ti_3C_2 can be both observed in the composites.

Fig.1B shows the FT-IR spectra of these raw and composite materials. No peaks are observed in $\text{Ti}_3\text{C}_2\text{T}_x$ FT-IR spectrum though the C-C and C-Ti bonds are contained. As pure

Ti₃C₂ shows no IR peaks, the IR signals in the composites are obviously from g-C₃N₄. Specifically, the peaks between 3500 and 3000 cm⁻¹ are assigned to the N-H stretching (=NH or -NH₂) and the series peaks near 800 and between 1650 and 1250 cm⁻¹ come from s-triazine derivatives.^{47, 48} The FT-IR spectra of composite samples treated with different annealing conditions are nearly identical to that of pure g-C₃N₄, indicating that g-C₃N₄ and Ti₃C₂ are not chemically bonded.

The morphologies of raw and composites samples were observed by the scanning electronic microscope (SEM) images (Figure 2). The morphology of g-C₃N₄ is bulky, as shown in Figure 2A, whereas the typical 2D nanosheets stacks structure can be clearly observed for the HF etched Ti₃C₂T_x (Figure 2B). When g-C₃N₄ and Ti₃C₂T_x are mixed in a pestle and mortar, the specific morphology characteristics of both g-C₃N₄ and Ti₃C₂T_x still remain, shown Figure 2C, D, E. Although the composites contain more g-C₃N₄ than Ti₃C₂T_x, Ti₃C₂T_x particles are not completely covered by g-C₃N₄ particles. It is noteworthy that annealing of g-C₃N₄/Ti₃C₂T_x composite at 200°C, in N₂ or in air, does not destroy the 2D structure of Ti₃C₂T_x.

Figure 3 shows the X-ray photoelectron spectroscopy (XPS) results of raw and composites materials to study any changes in the surface termination groups of Ti₃C₂ after annealing. The ratio of the peak areas of Ti 2p_{3/2} and Ti 2p_{1/2} is controlled 2 : 1 (Figure 3A). T_x represents the surface termination groups, such as -F, -O and -OH. The peaks at 456 eV and 461 eV are the combinations of the Ti-F bonds, Ti-O bonds and Ti-OH bonds.^{49, 50} The ratio of Ti-T_x bond and Ti-C bond signals varies significantly suggesting the change in the surface termination groups. The Ti-C bond signal remains the same while the Ti-T_x bonds decrease after the

annealing processes are applied. By comparing the peak fitting results of different samples, the increasing signals at 459 eV and 465 eV reflect the decreasing amount of the surface termination groups. The fact that the sample annealed in air exhibits less Ti-T_x bonds than the sample annealed in N₂ can be attributed to the presence of O₂. By comparing the O 1s region spectra, the Ti-O-Ti peak at 530 eV and the Ti-OH peak at 532 eV are separated to identify the -O termination groups (Figure 3B). The proportion of the Ti-O-Ti structure⁵⁰⁻⁵³ as a measure of TiO₂ phase¹⁶ increases after annealing in N₂ and air, though crystalline TiO₂ signal is not detected in the XRD patterns (Figure 1A) g-C₃N₄/Ti₃C₂T_x annealed in air contains the most Ti-O-Ti bonds, g-C₃N₄/Ti₃C₂T_x annealed in N₂ comes second and g-C₃N₄/Ti₃C₂T_x without post treatment contains the least, whereas the proportion of Ti-OH bonds show an opposite ranking.

Table 1 shows the contents of different elements extracted from the XPS spectra to monitor the change of Ti : F ratio upon the annealing methods. The sample annealed in air displays the highest Ti : F ratio confirming the decreasing of the -F terminations after thermal treatment. Previously, Li et al⁴⁰ and Hope et al³⁸ confirmed that the -OH groups on the surface of Ti₃C₂ react as equation (1), when it is heated at 200°C. This reaction mainly takes place during the annealing process resulting in the increasing of Ti-O-Ti groups with the decreasing of Ti-OH.

The presence of O₂ increased the ratio of Ti-O-Ti during annealing, according to the higher Ti-O-Ti content when annealed in air. Meanwhile, the content of -F terminations decreased for both annealing processes regardless of the atmosphere, N₂ or air, at a relatively low temperature (200°C). However, the mechanism corresponding to -F removal was still

unclear. The samples annealed in air demonstrate the least -F ratio and the most Ti-O-Ti ratio comparing the parallel samples, though the exact ratio of Ti-O-Ti, Ti-OH, and Ti-F cannot be identified by the XPS spectra.

The morphology of g-C₃N₄ with 30% Ti₃C₂ annealed in air is assessed via HRTEM in Figure S1. Low magnification image demonstrates the hybrid of g-C₃N₄ and Ti₃C₂. The layered structure of g-C₃N₄ is clearly shown. The high magnification image displays the interface of the hybrid. As g-C₃N₄ and Ti₃C₂ layers can be observed obviously, the heterojunction interface is considered formed.

3.2 UV-Vis DRS characterization

Figure 4 displays the UV-vis diffuse reflectance spectra (UV-vis DRS) of raw and composites materials; UV-vis DRS is a widely adopted method in investigating the optical absorption in semiconductor-based photo-catalysis. The fact that the Ti₃C₂T_x exhibits no obvious absorption edge is attributed to its metallic nature.³³ On the other hand, the pure g-C₃N₄ and the g-C₃N₄/Ti₃C₂ composites exhibit an absorption band around the wavelength of 460 nm reflecting the bandgap of g-C₃N₄, and this bandgap is insensitive to the annealing process.⁵⁴ The presence of the black Ti₃C₂T_x merely increases the absorption baseline in the composites as reported previously.³³ Though the absorption edges changed slightly, no obvious red shift or shoulder absorption are observed. Thus the band gaps of the composites do not change. In view of this, light absorption is a negligible factor in discussing the resulting HER performance by these g-C₃N₄/Ti₃C₂ composites.

3.3 Photocatalytic performance of g-C₃N₄/Ti₃C₂ composites

These composite materials were then tested in photocatalysis for water splitting. Figure 6A compares HER results using g-C₃N₄/Ti₃C₂ composites in which Ti₃C₂ functions as co-catalysis. The photo-catalytic H₂ productions by the g-C₃N₄/Ti₃C₂ composites are evaluated with visible light irradiation ($\lambda > 400$ nm). The maximum H₂ production rate of the composite material without annealing is merely 5.3 $\mu\text{mol/h/g.cat}$ after optimization the ratio of Ti₃C₂ in the composite to 30%. After annealing this composite at 200°C in N₂, the H₂ production increased to 7.8 $\mu\text{mol/h/g.cat}$, which is 45.2% higher than without annealing at the same ratio of g-C₃N₄ to Ti₃C₂. Moreover, the H₂ production of g-C₃N₄ with 30% Ti₃C₂ after annealing in air can achieve 10.9 $\mu\text{mol/h/g.cat}$, which is further 41.06% higher than that of the sample annealed in N₂ and 104.84% higher than without annealing. However, the best HER performance is achieved at different mass ratios for these composites samples (Figure S2). The best performance for g-C₃N₄/Ti₃C₂ composites annealed in N₂ is achieved at a ratio of 70%, with an HER reaching 14.2 $\mu\text{mol/h/g.cat}$, which is 166% higher than the best performance of non-annealed composite. Importantly, the HER performance of the composite of g-C₃N₄ with 190% Ti₃C₂ annealed in air gives the best performance among all, with a H₂ production as high as 88 $\mu\text{mol/h/g.cat}$, which is a 15-fold increasing compared the best non-annealed composite, compared with 53.3 $\mu\text{mol/h/g.cat}$ using Co₂P as cocatalyst.⁷ Meanwhile, the highest AQY achieves 1.27%, the same order of magnitude as reported.⁶ What is more, the Pt cocatalyst is also compared in the system (Figure S3), g-C₃N₄ with 3% Pt demonstrates the best performance for 56.2 $\mu\text{mol/h/g.cat}$, which is lower than that of g-C₃N₄ with 190% Ti₃C₂ annealed in air. The stability of the hybrid is also considered, there is a 64% decrease of hydrogen evolution rate for g-C₃N₄ with 30% Ti₃C₂ annealed in air after

4 cycles and 24 h of tests. This is mainly caused by the separation of g-C₃N₄ and Ti₃C₂. The heterojunction interface disappears though the XRD spectra (Figure S4) show no obvious differences before and after the photocatalytic activity tests.

Figure 6B shows the photoluminescence (PL) spectra of the samples used in HER measurements. These PL spectra exhibit an identical emission peak at 463 nm. The bare g-C₃N₄ shows the strongest PL signal due to the spontaneous recombination of the photogenerated electron-hole pairs. The composites of Ti₃C₂/g-C₃N₄ containing 30% Ti₃C₂ exhibit reduced PL intensity owing to the prevention of recombination of the photogenerated electron-hole pairs by Ti₃C₂, which is one of the reasons of enhanced HER activity.

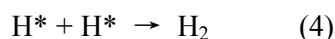
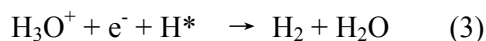
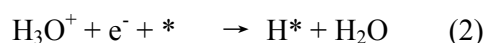
Table 2 lists the specific surface area obtained from the BET measurements of the g-C₃N₄ with 30% Ti₃C₂ samples. The surface area of these samples are coincident with their HER performance. Specifically, the annealed samples have higher specific surface area than without annealing, and the performances of photocatalysis activity of the formers are also better than that of the latter. The higher specific surface area provides more active sites for the HER reactions including the depleting of the photogenerated holes by the triethanolamine on the surface of g-C₃N₄ and/or the H₂ production on the surface of Ti₃C₂T_x.

3.4 Photocatalytic and HER mechanism

The photocatalyst g-C₃N₄ is excited by the white light and then electron-hole pairs are generated. The electrons gather on Ti₃C₂ through the ohmic contact between g-C₃N₄ with the semiconductor nature and the metallic MXenes, resulting in a negative shift of the Fermi level,^{33, 34} and this will improve the separation of the electron-hole pairs. The holes left on the semiconductor are reduced by the electron donor or electron scavenger, triethanolamine. As

shown in Table 1, the increasing specific surface area provides more active sites to sacrifice the holes and separates the electron-hole pairs as well.

We consider the reaction mechanism of the HER on the surface of the MXenes is the same as the one in electrocatalysis because of the same active sites and electron with high energy. Thus, the H₂ production react as the following Equation(2), (3) and (4) as the three main steps as reported:^{55, 56}



The * represent the active sites for the HER and are considered to be the -O surface termination groups on the surface of Ti₃C₂ here.^{33, 57} Thus H₃O⁺ ion can be adsorbed on the -O surface terminations and combine with an electron to form an H atom, which is known as the Volmer reaction. At the same active site, H atom combines another H₃O⁺ ion from water and an electron from Ti₃C₂ to form a H₂ molecule as in equation (2), which is called the Heyrovsky mechanism. Two H atoms on the active sites form a H₂ molecule which is considered the Tafel mechanism in equation (3). Hydrogen molecules form with the presence of photogenerated electrons and H₃O⁺ ions at the active sites, the -O surface terminations. Therefore more -O surface terminations improve the HER performance and the g-C₃N₄/Ti₃C₂ composite annealed in the air exhibits the best photocatalytic activity.

3.5 DFT calculations

Figure 7A showed the top and side views of the Ti₃C₂ structure. a, b and c represent the space sites for termination groups on the surface of Ti₃C₂. a were on top of C atoms, b were

over the surface Ti atoms and c were over the mid-layered Ti atoms. The -O and -F terminations occupied the c sites and -OH termination groups were not considered because of is indirectly connected to the primary step in HER mechanism.⁵⁸ Figure 7B, C and D demonstrated the Gibbs free energies (ΔG_H) of bare, -O and -F terminated Ti_3C_2 with the atomic H coverage of 25% and 50%, respectively. The near-zero $|\Delta G_H|$ which mean the high HER catalytic ability was desirable. $|\Delta G_H|$ of all structures were exhibited in Table S1 in details. -F terminated Ti_3C_2 demonstrated a high $|\Delta G_H|$ value and the best structure for HER co-catalyst was Ti_3C_2 with -O terminations, of which the $|\Delta G_H|$ was as low as 0.01 eV. $|\Delta G_H|$ of typical HER co-catalyst Pt(111) was 0.09 eV and MoS_2 was 0.08 eV,^{59, 60} both were much higher than that of Ti_3C_2 with -O terminations. Thus -O terminated Ti_3C_2 was a better replacement of noble metal Pt as the co-catalyst for HER. The $|\Delta G_H|$ of 25% atomic H covered Ti_3C_2 with -O terminations was much lower than that of 50% atomic H covered Ti_3C_2 . This was mainly caused by the decrease of the active site for HER, thus 25% atomic H coverage of Ti_3C_2 with -O terminations showed the best catalytic ability for HER.

Conclusions

In summary, the two-dimensional titanium carbide MXene Ti_3C_2 is investigated as a co-catalyst for its HER activity by variation of the mixed ratio of g- C_3N_4 with Ti_3C_2 and by modifying the surface termination groups on the surface of Ti_3C_2 . The best HER performance is obtained at the g- C_3N_4 / Ti_3C_2 ratio of 190% followed by annealing in air in muffle furnace with a high H_2 production of 88 $\mu\text{mol/h/g.cat}$. **The AQY achieves as high as 1.27%.** The increased HER is attributed to the higher specific surface area providing more active sites and the -O surface terminations of Ti_3C_2 , which improved the separation of the electron-hole pairs.

Our findings illustrate that Ti_3C_2 MXene can be used as co-catalyst in g- C_3N_4 -based photocatalytic HER, thus paving the way for the commercialization of MXenes for solar energy conversion. The DFT calculations showed that the Ti_3C_2 with -O surface terminations and 25% covered H atoms demonstrated the lowest free energy at 0.011eV, and also confirmed the experimental result that Ti_3C_2 with -O surface termination shows the best HER activity as co-catalyst in photocatalysis.

Conflict of interest

There are no conflicts to declare.

Acknowledgements

This work is supported by the Natural Science Foundation of China (No. 11574111 to X-F.W.), Natural Science Foundation of Jilin Province (No. 20160101303JC to X-F.W.). Acknowledgements to Prof. Yury Gogotsi and the Thousand Talents Program (China).

References

1. H. Yu, P. Xiao, P. Wang and J. Yu, *Applied Catalysis B: Environmental*, 2016, **193**, 217-225.
2. H. Pan, Y.-W. Zhang, V. B. Shenoy and H. Gao, *ACS Catalysis*, 2011, **1**, 99-104.
3. X. Wang, K. Maeda, A. Thomas, K. Takanabe, G. Xin, J. M. Carlsson, K. Domen and M. Antonietti, *Nature materials*, 2009, **8**, 76-80.
4. W. J. Ong, L. L. Tan, Y. H. Ng, S. T. Yong and S. P. Chai, *Chemical reviews*, 2016, **116**, 7159-7329.
5. W.-J. Ong, *Frontiers in Materials*, 2017, **4**, 11.
6. D. Zeng, W.-J. Ong, H. Zheng, M. Wu, Y. Chen, D.-L. Peng and M.-Y. Han, *Journal of Materials Chemistry A*, 2017, **5**, 16171-16178.
7. D. Zeng, W.-J. Ong, Y. Chen, S. Y. Tee, C. S. Chua, D.-L. Peng and M.-Y. Han, *Particle & Particle Systems Characterization*, 2018, **35**, 1700251.
8. D. Zeng, P. Wu, W.-J. Ong, B. Tang, M. Wu, H. Zheng, Y. Chen and D.-L. Peng, *Applied Catalysis B: Environmental*, 2018, **233**, 26-34.
9. D. Zeng, W. Xu, W.-J. Ong, J. Xu, H. Ren, Y. Chen, H. Zheng and D.-L. Peng, *Applied Catalysis B: Environmental*, 2018, **221**, 47-55.
10. M. Naguib, M. Kurtoglu, V. Presser, J. Lu, J. Niu, M. Heon, L. Hultman, Y. Gogotsi and M. W. Barsoum, *Advanced materials*, 2011, **23**, 4248-4253.
11. M. Naguib, V. N. Mochalin, M. W. Barsoum and Y. Gogotsi, *Advanced materials*, 2014, **26**, 992-1005.
12. B. Anasori, M. R. Lukatskaya and Y. Gogotsi, *Nature Reviews Materials*, 2017, **2**, 16098.
13. Y. Dall'Agnese, P. L. Taberna, Y. Gogotsi and P. Simon, *The journal of physical chemistry letters*, 2015, **6**, 2305-2309.
14. C. J. Zhang, B. Anasori, A. Seral-Ascaso, S. H. Park, N. McEvoy, A. Shmeliov, G. S. Duesberg, J. N. Coleman, Y. Gogotsi and V. Nicolosi, *Advanced materials*, 2017, **29**.
15. M.-Q. Zhao, M. Torelli, C. E. Ren, M. Ghidui, Z. Ling, B. Anasori, M. W. Barsoum and Y. Gogotsi, *Nano Energy*, 2016, **30**, 603-613.
16. M. Naguib, J. Come, B. Dyatkin, V. Presser, P.-L. Taberna, P. Simon, M. W. Barsoum and Y. Gogotsi, *Electrochemistry Communications*, 2012, **16**, 61-64.
17. M. Q. Zhao, X. Xie, C. E. Ren, T. Makaryan, B. Anasori, G. Wang and Y. Gogotsi, *Advanced materials*, 2017, **29**.
18. S.-Y. Lin and X. Zhang, *Journal of Power Sources*, 2015, **294**, 354-359.
19. L. Li, M. Zhang, X. Zhang and Z. Zhang, *Journal of Power Sources*, 2017, **364**, 234-241.
20. Q. Fu, J. Wen, N. Zhang, L. Wu, M. Zhang, S. Lin, H. Gao and X. Zhang, *RSC Advances*, 2017, **7**, 11998-12005.
21. F. Shahzad, M. Alhabeab, C. B. Hatter, B. Anasori, H. S. Man, C. M. Koo and Y. Gogotsi, *Science*, 2016, **353**, 1137.
22. X. Li, X. Yin, M. Han, C. Song, H. Xu, Z. Hou, L. Zhang and L. Cheng, *Journal of Materials Chemistry C*, 2017, **5**, 4068-4074.

23. M. Han, X. Yin, H. Wu, Z. Hou, C. Song, X. Li, L. Zhang and L. Cheng, *ACS applied materials & interfaces*, 2016, **8**, 21011-21019.
24. M. Ming, Y. Ren, M. Hu, Y. Zhang, T. Sun, Y. Ma, X. Li, W. Jiang, D. Gao, J. Bi and G. Fan, *Applied Catalysis B: Environmental*, 2017, **210**, 462-469.
25. Y. Ying, Y. Liu, X. Wang, Y. Mao, W. Cao, P. Hu and X. Peng, *ACS applied materials & interfaces*, 2015, **7**, 1795-1803.
26. Q. Peng, J. Guo, Q. Zhang, J. Xiang, B. Liu, A. Zhou, R. Liu and Y. Tian, *Journal of the American Chemical Society*, 2014, **136**, 4113-4116.
27. Z. W. Seh, K. D. Fredrickson, B. Anasori, J. Kibsgaard, A. L. Strickler, M. R. Lukatskaya, Y. Gogotsi, T. F. Jaramillo and A. Vojvodic, *ACS Energy Letters*, 2016, **1**, 589-594.
28. M. Khazaei, M. Arai, T. Sasaki, C.-Y. Chung, N. S. Venkataramanan, M. Estili, Y. Sakka and Y. Kawazoe, *Advanced Functional Materials*, 2013, **23**, 2185-2192.
29. Y. Xie and P. Kent, *Physical Review B*, 2013, **87**, 235441.
30. Y. Gao, L. Wang, A. Zhou, Z. Li, J. Chen, H. Bala, Q. Hu and X. Cao, *Materials Letters*, 2015, **150**, 62-64.
31. C. Peng, X. Yang, Y. Li, H. Yu, H. Wang and F. Peng, *ACS applied materials & interfaces*, 2016, **8**, 6051-6060.
32. H. Wang, R. Peng, Z. D. Hood, M. Naguib, S. P. Adhikari and Z. Wu, *ChemSusChem*, 2016, **9**, 1490-1497.
33. J. Ran, G. Gao, F. T. Li, T. Y. Ma, A. Du and S. Z. Qiao, *Nature communications*, 2017, **8**, 13907.
34. M. Shao, Y. Shao, J. Chai, Y. Qu, M. Yang, Z. Wang, M. Yang, W. F. Ip, C. T. Kwok, X. Shi, Z. Lu, S. Wang, X. Wang and H. Pan, *Journal of Materials Chemistry A*, 2017, **5**, 16748-16756.
35. T. Su, R. Peng, Z. D. Hood, M. Naguib, I. N. Ivanov, J. K. Keum, Z. Qin, Z. Guo and Z. Wu, *ChemSusChem*, 2018, **11**, 688-699.
36. .
37. N. Li, X. Chen, W. J. Ong, D. R. MacFarlane, X. Zhao, A. K. Cheetham and C. Sun, *ACS Nano*, 2017, **11**, 10825-10833.
38. M. A. Hope, A. C. Forse, K. J. Griffith, M. R. Lukatskaya, M. Ghidui, Y. Gogotsi and C. P. Grey, *Physical chemistry chemical physics : PCCP*, 2016, **18**, 5099-5102.
39. Y. Xie, M. Naguib, V. N. Mochalin, M. W. Barsoum, Y. Gogotsi, X. Yu, K. W. Nam, X. Q. Yang, A. I. Kolesnikov and P. R. Kent, *Journal of the American Chemical Society*, 2014, **136**, 6385-6394.
40. Z. Li, L. Wang, D. Sun, Y. Zhang, B. Liu, Q. Hu and A. Zhou, *Materials Science and Engineering: B*, 2015, **191**, 33-40.
41. M. Naguib, O. Mashtalir, M. R. Lukatskaya, B. Dyatkin, C. Zhang, V. Presser, Y. Gogotsi and M. W. Barsoum, *Chemical communications*, 2014, **50**, 7420-7423.
42. X. Lu, K. Xu, P. Chen, K. Jia, S. Liu and C. Wu, *J. Mater. Chem. A*, 2014, **2**, 18924-18928.
43. G. Kresse and J. Furthmüller, *Physical Review B Condensed Matter*, 1996, **54**, 11169.
44. G. Kresse and D. Joubert, *Physical Review B*, 1999, **59**, 1758.

45. J. P. Perdew, J. A. Chevary, S. H. Vosko, K. A. Jackson, M. R. Pederson, D. J. Singh and C. Fiolhais, *Physical Review B Condensed Matter*, 1992, **46**, 6671.
46. J. P. Perdew and Y. Wang, *Physical Review B Condensed Matter*, 1992, **45**, 13244.
47. Y. Li, J. Zhang, Q. Wang, Y. Jin, D. Huang, Q. Cui and G. Zou, *The Journal of Physical Chemistry B*, 2010, **114**, 9429-9434.
48. B. V. Lotsch, M. Dobliger, J. Sehnert, L. Seyfarth, J. Senker, O. Oeckler and W. Schnick, *Chemistry*, 2007, **13**, 4969-4980.
49. C. E. Ren, M.-Q. Zhao, T. Makaryan, J. Halim, M. Boota, S. Kota, B. Anasori, M. W. Barsoum and Y. Gogotsi, *ChemElectroChem*, 2016, **3**, 689-693.
50. A. Lipatov, M. Alhabeab, M. R. Lukatskaya, A. Boson, Y. Gogotsi and A. Sinitskii, *Advanced Electronic Materials*, 2016, **2**, 1600255.
51. B. Ahmed, D. H. Anjum, M. N. Hedhili, Y. Gogotsi and H. N. Alshareef, *Nanoscale*, 2016, **8**, 7580-7587.
52. O. Mashtalir, K. M. Cook, V. N. Mochalin, M. Crowe, M. W. Barsoum and Y. Gogotsi, *J. Mater. Chem. A*, 2014, **2**, 14334-14338.
53. T. Zhang, L. Pan, H. Tang, F. Du, Y. Guo, T. Qiu and J. Yang, *Journal of Alloys and Compounds*, 2017, **695**, 818-826.
54. Y. Kang, Y. Yang, L. C. Yin, X. Kang, G. Liu and H. M. Cheng, *Advanced materials*, 2015, **27**, 4572-4577.
55. J. Deng, P. Ren, D. Deng, L. Yu, F. Yang and X. Bao, *Energy Environ. Sci.*, 2014, **7**, 1919-1923.
56. B. Conway and B. Tilak, *Electrochimica Acta*, 2002, **47**, 3571-3594.
57. C. Ling, L. Shi, Y. Ouyang, Q. Chen and J. Wang, *Advanced science*, 2016, **3**, 1600180.
58. M. Pandey and K. S. Thygesen, *The Journal of Physical Chemistry C*, 2017, **121**, 13593-13598.
59. J. K. Nørskov, T. Bligaard, A. Logadottir, J. R. Kitchin, J. G. Chen, S. Pandelov and U. Stimming, *Journal of The Electrochemical Society*, 2005, **152**, J23.
60. J. Bonde, P. G. Moses, T. F. Jaramillo, J. K. Nørskov and I. Chorkendorff, *Faraday discussions*, 2009, **140**, 219-231.

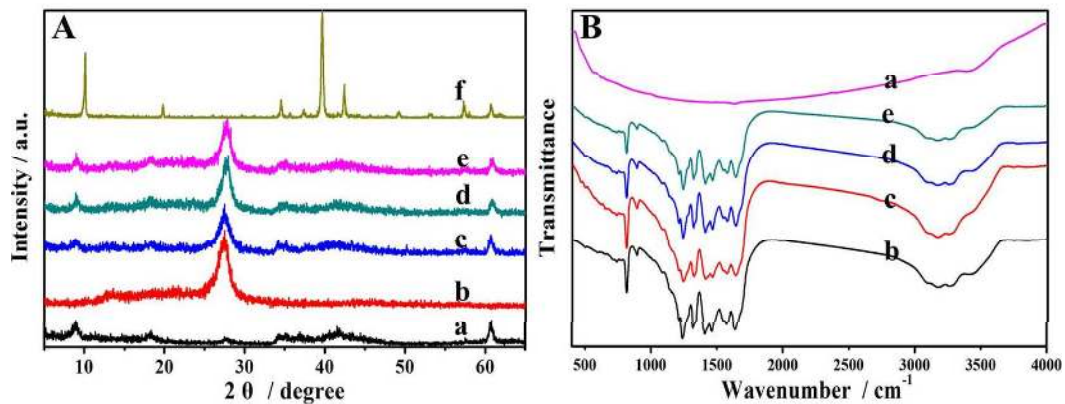


Figure 1. A) The XRD patterns of the two pure materials and the hybrids B) The FTIR spectra of the two pure materials and the composites. a) Ti₃C₂, b) g-C₃N₄, c) g-C₃N₄ with 30% Ti₃C₂, d) g-C₃N₄ with 30% Ti₃C₂ annealed in N₂, e) g-C₃N₄ with 30% Ti₃C₂ annealed in air and f) Ti₃AlC₂.

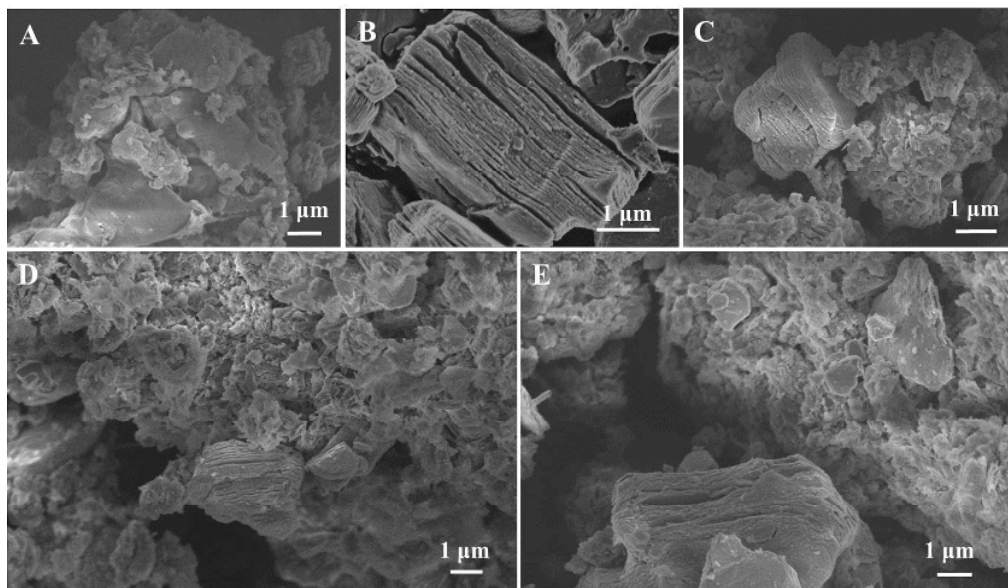


Figure 2. The SEM image of A) g-C₃N₄ B) Ti₃C₂ C) g-C₃N₄ with 30% Ti₃C₂ D) g-C₃N₄ with 30% Ti₃C₂ annealed in N₂ E) g-C₃N₄ with 30% Ti₃C₂ annealed in air.

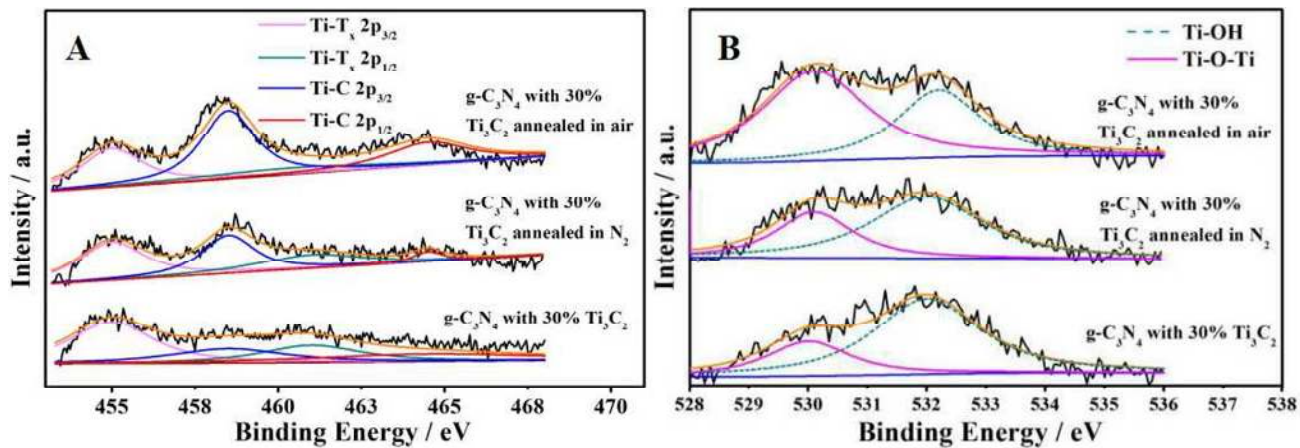


Figure 3. The XPS spectra of O 1s region (A) and Ti 2p region (B) for g-C₃N₄ with 30% Ti₃C₂, g-C₃N₄ with 30% Ti₃C₂ annealed in N₂ and g-C₃N₄ with 30% Ti₃C₂ annealed in air.

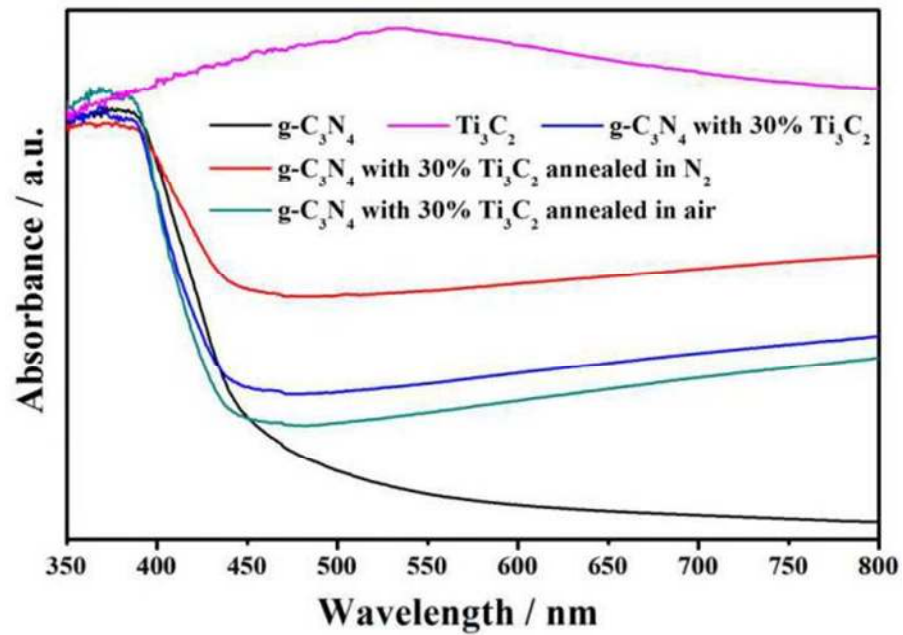


Figure 4. The DRS spectra of $g\text{-C}_3\text{N}_4$, Ti_3C_2 , $g\text{-C}_3\text{N}_4$ with 30% Ti_3C_2 , $g\text{-C}_3\text{N}_4$ with 30% Ti_3C_2 annealed in N_2 and $g\text{-C}_3\text{N}_4$ with 30% Ti_3C_2 annealed in air.

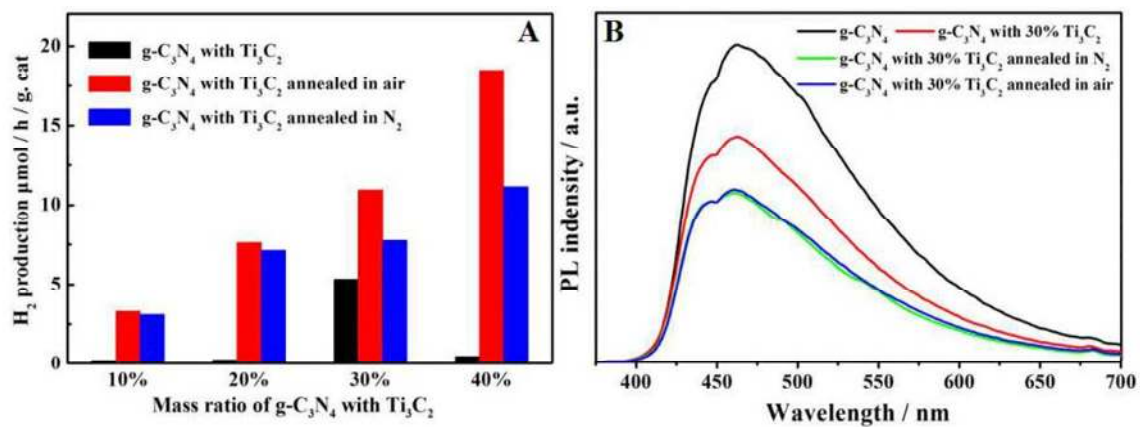


Figure 5. A) The production of g-C₃N₄, g-C₃N₄ with Ti₃C₂, g-C₃N₄ with Ti₃C₂ annealed in N₂ and g-C₃N₄ with Ti₃C₂ annealed in air at different ratios B) The PL spectra at an excitation wavelength of 340 nm.

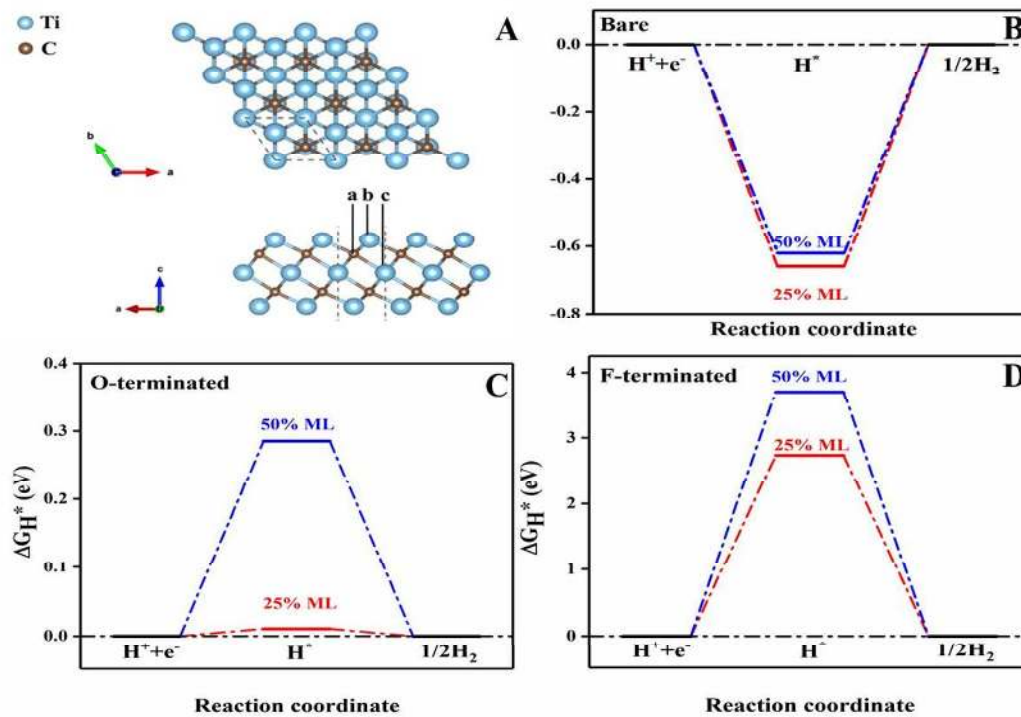


Figure 6. A) The top view and side view of Ti_3C_2 , free energy of B) bare, C) -O terminated and D) -F terminated Ti_3C_2 with 25% and 50% coverages of atomic H.

Table 1. The XPS surveys of A) g - C₃N₄ B) g-C₃N₄ with 30% Ti₃C₂, C) g-C₃N₄ with 30% Ti₃C₂ annealed in N₂ and D) g-C₃N₄ with 30% Ti₃C₂ annealed in air.

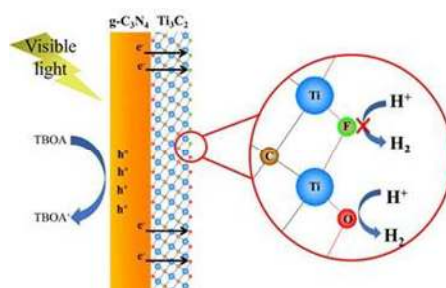
Samples	C	N	O	F	Ti
g-C ₃ N ₄	55.7	41	3.3		
g-C ₃ N ₄ with 30% Ti ₃ C ₂	54.3	36.5	5.9	2.1	1.2
g-C ₃ N ₄ with 30% Ti ₃ C ₂ annealed in N ₂	56.2	36.2	4.6	1.5	1.5
g-C ₃ N ₄ with 30% Ti ₃ C ₂ annealed in air	53.9	37.3	5.7	1.2	1.8

Table 2. The specific surface area for different samples.

Samples	BET m²/g
g-C ₃ N ₄	55
Ti ₃ C ₂	6
g-C ₃ N ₄ with 30% Ti ₃ C ₂	36
g-C ₃ N ₄ with 30% Ti ₃ C ₂ annealed in N ₂	50
g-C ₃ N ₄ with 30% Ti ₃ C ₂ annealed in air	49

Table of contents

Oxidized Surface Groups on MXenes for Efficient Photocatalytic Hydrogen Evolution



Supporting Information

g-C₃N₄/Ti₃C₂T_x(MXenes) Composite with Oxidized Surface Groups for Efficient Photocatalytic Hydrogen Evolution

Yuliang Sun^a, Di Jin^a, Yuan Sun^a, Xing Meng^{a,c,*}, Yu Gao^a, Yohan Dall'Agnese^a,
Gang Chen^{a,b}, Xiao-Feng Wang^{a,*}

^a*Key Laboratory of Physics and Technology for Advanced Batteries (Ministry of Education), College of Physics, Jilin University, Changchun 130012, PR China*

^b*State Key Laboratory of Superhard Materials, Jilin University, Changchun 130012, PR China*

^c*A. J. Drexel Nanomaterials Institute, and Department of Materials Science and Engineering, Drexel University, Philadelphia, Pennsylvania 19104, United States*

The images of HRTEM of the composite were showed in supporting information. The HER of different ratios and annealing method between g-C₃N₄ and Ti₃C₂ and Δ GH (eV) of different terminated Ti₃C₂ were also demonstrated.

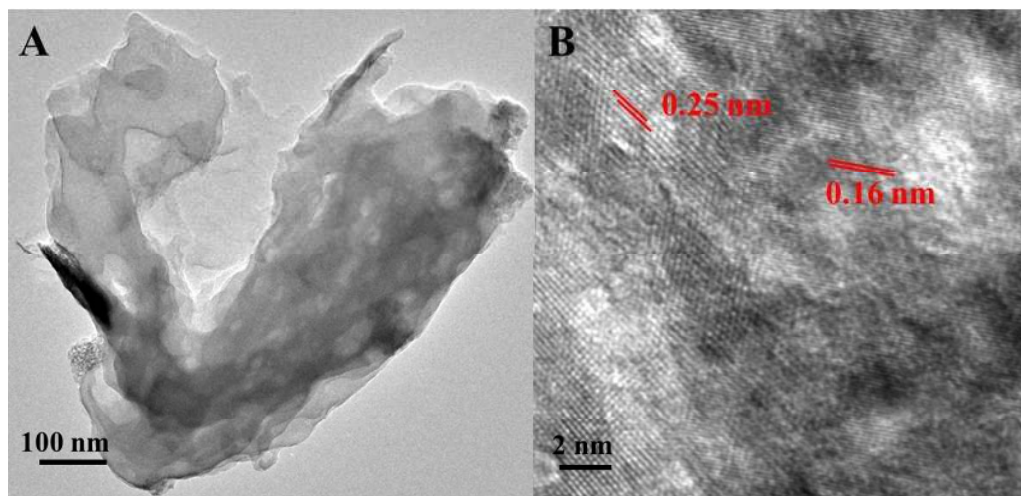


Figure S1. The HRTEM image of g-C₃N₄ with 30% Ti₃C₂ annealed in air for A) low and B) high magnification.

Figure S1 showed the HRTEM image of the hybrid. The interface between g-C₃N₄ and Ti₃C₂ could be observed obviously.

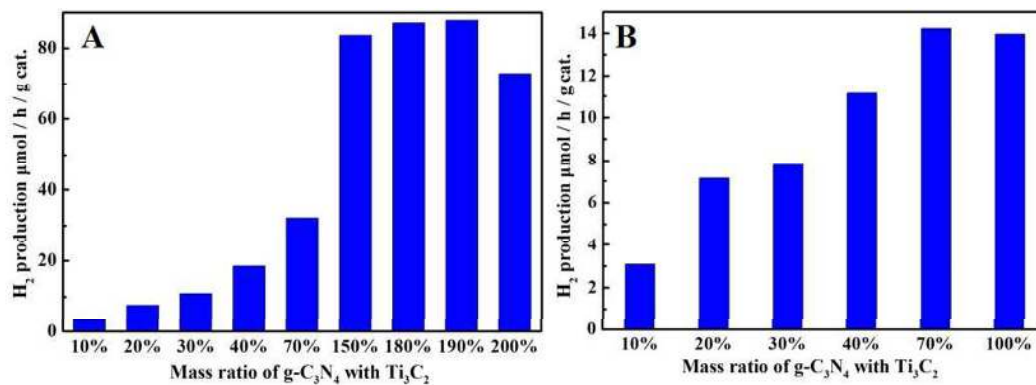


Figure S2. The HER of A) g-C₃N₄ with Ti₃C₂ annealed in N₂ and B) g-C₃N₄ with Ti₃C₂ annealed in air at different ratios.

As shown in Figure S2, the mass ratio of $g\text{-C}_3\text{N}_4$ with Ti_3C_2 at 190% annealed in air demonstrated the best performance for hydrogen evolution while that at 70% annealed in N_2 did.

In Figure S3, $g\text{-C}_3\text{N}_4$ with 3% Pt as cocatalyst demonstrated the best H_2 production, which achieved $56.2 \mu\text{mol/h/g.cat}$ and lower than that of $g\text{-C}_3\text{N}_4$ with 190% Ti_3C_2 annealed in air.

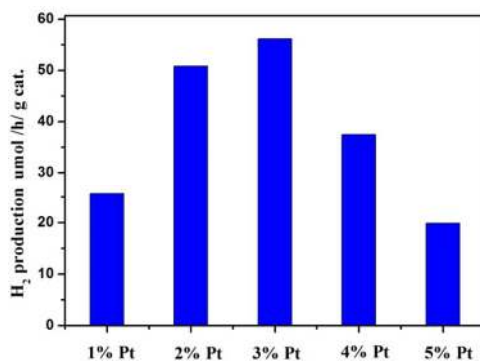


Figure S3. The HER of $g\text{-C}_3\text{N}_4$ with Pt at different ratios.

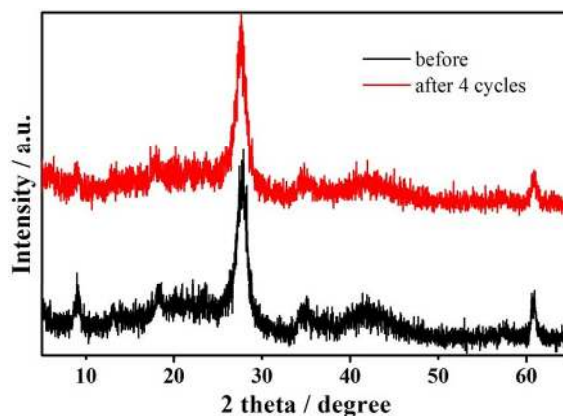

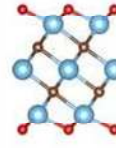
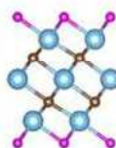


Figure S4. The XRD spectra of $g\text{-C}_3\text{N}_4$ with 30% Ti_3C_2 annealed in air before and after 4 cycles.

Though the separation of g-C₃N₄ and Ti₃C₂ after tests, no obvious differences were shown between the XRD spectra of g-C₃N₄ with 30% Ti₃C₂ annealed in air before and after 4 cycles.

Table S1 displayed the ΔG_H of Ti₃C₂ with different termination groups. ΔG_H of -F terminations were much higher than that of -O, thus -O terminations showed a better photocatalysis activity of hydrogen evolution.

Table S1. ΔG_H (eV) of different terminated Ti₃C₂ with different atomic H coverage

System	structure	Site	θ_H (ML)	ΔG_H (eV)
Bare		-	25%	-0.659
			50%	-0.626
O-Ti ₃ C ₂		c	25%	0.011
			50%	0.285
F-Ti ₃ C ₂		c	25%	2.740
			50%	3.705

g-C₃N₄/Ti₃C₂T_x(MXenes) Composite with Oxidized Surface Groups for Efficient Photocatalytic Hydrogen Evolution

Yuliang Sun^a, Di Jin^a, Yuan Sun^a, Xing Meng^{a,c,*}, Yu Gao^a, Yohan Dall'Agnesse^a, Gang Chen^{a,b}, Xiao-Feng Wang^{a,*}

^a*Key Laboratory of Physics and Technology for Advanced Batteries (Ministry of Education), College of Physics, Jilin University, Changchun 130012, PR China*

^b*State Key Laboratory of Superhard Materials, Jilin University, Changchun 130012, PR China*

^c*A. J. Drexel Nanomaterials Institute, and Department of Materials Science and Engineering, Drexel University, Philadelphia, Pennsylvania 19104, United States*

*Xiao-Feng Wang E-mail: xf_wang@jlu.edu.cn

*Xing Meng E-mail: mengxing@jlu.edu.cn

Abstract

Ti₃C₂T_x is a 2-dimensional titanium carbide material featuring outstanding electrochemical properties. In spite of this, application of Ti₃C₂T_x as co-catalyst in photo-catalysis is rarely under explored probably because of its metallic nature and the hydrophilic surface. Given that

$\text{Ti}_3\text{C}_2\text{T}_x$ with different surface terminations exhibits large differences in catalytic, electrochemical and chemical properties, we demonstrate improvement of the photocatalytic activity of $\text{Ti}_3\text{C}_2\text{T}_x$ as a co-catalyst by annealing a composite of carbon nitride and $\text{Ti}_3\text{C}_2\text{T}_x$. $\text{Ti}_3\text{C}_2\text{T}_x$ with the oxygen terminated surface improves the separation of electron-hole pairs resulting in 105% enhancement in production ratio in hydrogen evolution as compared with the control samples. The best hydrogen production performance achieves as high as 88 $\mu\text{mol/h/g.cat}$. The apparent quantum yield (AQY) achieves as high as 1.27%. The DFT calculations also demonstrate a better hydrogen evolution on Ti_3C_2 with oxygen surface termination.

Key words: MXenes, photocatalysis, surface termination groups, hydrogen evolution, DFT calculation.

Introduction

The traditional energy sources such as coal, oil and natural gas are unsustainable and will leave an energy gap of 14TW by the year of 2050. To fill that energy gap, solar energy is considered the only available renewable energy resource with such a potential. Photocatalytic hydrogen evolution from water is an effective way to convert solar energy into chemical energy that is much easy to store. Semiconductor-based photocatalysts can split water into hydrogen and oxygen under the presence of co-catalysts, which are normally noble metals such as Pt, Ru, Rh, Pd. Among the semiconductors being developed nowadays, 2-dimensional (2D) photocatalyst g- C_3N_4 is promising because of its merits such as high stability, large surface area, non-toxicity and suitable band gap.¹⁻³ To improve the

photocatalytic activity of $g\text{-C}_3\text{N}_4$, various means are reported, including nanoarchitecture design, elemental doping, copolymerization and heterojunction nanostructures design.⁴ The noble-metal-free photocatalytic hydrogen evolution is also investigated such as metal chalcogenide, metal phosphide, metal oxide or even graphene to replace the high cost noble metal cocatalyst.⁵⁻⁹ Zeng et al achieves $535.7 \mu\text{mol/g/h}$ with Ni_{12}P_5 as cocatalyst⁶ and $474.7 \mu\text{mol/g/h}$ with Ni_2P .⁹

MXenes are a new family of 2D nanostructure materials, initially reported in 2011.¹⁰ MXenes are prepared from MAX phase by etching the A-layer (usually Al) with strong acid solutions such as HF or LiF/HCl. MXenes have a general formula of $\text{M}_{n+1}\text{X}_n\text{T}_x$ ($n = 1-3$), in which M represents an early transition metal, e.g., Ti, V, Nb, Ta, Mo, X is carbon and/or nitrogen, and T_x stands for the surface termination groups such as -O, -F and -OH.^{11, 12} MXenes have been applied to different fields including energy storage,¹³⁻²⁰ electromagnetic interference shielding,²¹⁻²³ water purification and catalysis for the electronic.²⁴⁻²⁷

The photo- and electro-catalytic properties of MXenes were predicted by the density functional theory(DFT) calculations.^{28, 29} Moreover, Mo_2CT_x and Ti_2CT_x were already investigated in electro-catalytic hydrogen evolution reaction (HER).²⁷ Mo_2CT_x exhibits good performance in stability, hydrogen evolution activity, and lower over potential. Nanocomposites of semiconductors and MXene, e.g., $\text{TiO}_2/\text{Ti}_3\text{C}_2$ were hydro-thermally synthesized to study their catalytic activity.³⁰ As a result, methyl orange(MO) is photocatalytic degraded in the presence of such composites when NaBF_4 is used to control the morphology of the composite.³¹ $\text{TiO}_2/\text{Ti}_3\text{C}_2\text{T}_x$, $\text{TiO}_2/\text{Ti}_2\text{CT}_x$ and $\text{TiO}_2/\text{Nb}_2\text{CT}_x$ composites have been tested as photo-catalysts for hydrogen production. Among these, $\text{TiO}_2/\text{Nb}_2\text{CT}_x$

exhibits the best performance.³² Besides, CdS/Ti₃C₂T_x was also synthesized by hydrothermal method, and Ti₃C₂T_x with small diameter but large surface area gives an excellent performance as the co-catalyst in photocatalytic HER.³³ Ti₂C is also found to exhibit co-catalysis in combination with the catalyst of g-C₃N₄ for HER.³⁴ Moreover, in situ oxidation of MXenes is also proved photocatalytic^{30, 35} and CO₂ conversion can also be achieved with the cocatalysis of MXenes.^{36, 37}

Surface terminations greatly affect the physicochemical properties of MXenes. Bare MXenes without termination groups have not been synthesized yet. Different synthetic methods produce different surface termination groups on MXenes. For example, MXenes etched by HF contain mainly -F terminations whereas those etched by LiF/HCl contain more -O terminations.³⁸ Post-treatment on as-prepared MXenes, however, alters the composition of the surface terminations, e.g., the -F terminations can be replaced gradually by -O terminations in the air.³⁹ In view of this, MXenes with -F terminations are much unstable compared with that with other terminations. -OH terminations transform into -O terminations at 200°C as depicted by the following equation:⁴⁰



The DFT calculations suggest that -O terminations may give better Li-ion storage capacity or behave as the HER active sites.^{16, 33, 39} In fact, the free energy of Ti₃C₂ with -O terminations is much lower than that of Pt and thus Ti₃C₂ with -O terminations may become an efficient and low-cost alternative of Pt in HER.³³ The composition of surface termination groups is not controllable in synthesis, but is controllable with hydrothermal or thermal

treatment. The presence of O_2 alters the surface termination groups efficiently by oxidizing Ti into TiO_2 at a high annealing temperature.⁴¹

Herein, we hybridized the composite of $g-C_3N_4/Ti_3C_2T_x$ by a scalable process and tuned the surface chemistry of $Ti_3C_2T_x$ by post-annealing in both air and N_2 atmospheres. The composite is very easily hybridized by the mixing in a mortar without other process such as hydrothermal, which was really a fast way. The prepared $Ti_3C_2T_x$ is employed as co-catalyst with $g-C_3N_4$ photocatalyst for the HER. The -O surface terminations clearly enhance the amount of hydrogen produced at the active sites. This research paves a way to replace the high-cost and precious metal co-catalysts in HER and to accelerate the development of HER for renewable energy revolution. The DFT calculations are also done to demonstrate the HER activity for different surface termination groups.

Experimental section

2.1 The synthesis of $g-C_3N_4$ and Ti_3C_2 MXenes

For the synthesis of $g-C_3N_4$, NH_4Cl is used as a template. Briefly, 2 g of dicyandiamide powder and 10 g ammonium chloride are dissolved in 100 ml deionized water and stirred at $75^\circ C$ until the mixture is separated out. The mixture is then heated in a muffle furnace at $550^\circ C$ for 4 h, and at a rate of $5^\circ C/min$.⁴² A mortar is used to make the bulky $g-C_3N_4$ into powder.

$Ti_3C_2T_x$ MXenes is obtained from etching Ti_3AlC_2 (Forsman, 98%) in 49% HF. 1 g Ti_3AlC_2 is added into 10 ml 49% HF slowly with stirring at a rate of 200 rpm at room temperature for 24 h. The etched suspension is then washed by deionized water and

centrifuged until the pH value near 7. The black wet powder is dried in a vacuum oven at 60°C overnight.

2.2 The preparation of g-C₃N₄/Ti₃C₂T_x composites

The yellow g-C₃N₄ powder and the black Ti₃C₂T_x powder are mixed with a pestle and mortar at different ratios. To modify the Ti₃C₂ surface terminations, the mixtures are then annealed for one hour at 200°C either in a tube furnace under N₂ protection or in a muffle oven in air. The samples with a mass ratio of Ti₃C₂T_x and g-C₃N₄ controlled at 3 : 10 were selected for further characterization and labelled 30%.

2.3 Characterizations

To characterize the g-C₃N₄, Ti₃C₂ and the composites powders, the X-ray diffractometer (XRD, DX-2700B) is operated at 40 KV and 200mA with Cu K α radiation ($\lambda = 0.15406$ nm). Scanning electron microscopy (SEM, JSM-6700F) is used to observe the morphology of the samples. X-ray photoelectron spectroscopy (XPS, ESCALAB) analysis is conducted using a Mg-K α light source to confirm the element ratio of the samples. Specific surface area measurements (Kubo-X1000) are typically based on N₂ sorption with pretreatment at 60°C under the Brunauer-Emmer-Teller (BET) model. Photoluminescence emission spectra (PL) are determined using a fluorescence spectrometer (Shimadzu RF-5301) at the 340 nm excitation and the powder samples are tested directly. Fourier Transform infrared spectroscopy (FTIR, Vertex 70, Bruker, Germany) is used in a range of 400 to 4000 cm⁻¹ to record the spectra for samples. Ultraviolet-Visible diffuse reflectance spectra (UV-Vis DRS, Specord 210 plus, Analytikjena, Germany) are measured for the absorption of samples under UV-Vis light with an optics integrating sphere using BaSO₄ as the standard. High resolution

transmission electron microscopy (HRTEM, FEI Tecnai G2 F20) is used to observe the heterojunction interface between g-C₃N₄ and Ti₃C₂T_x.

2.4 Photocatalytic activity measurements

Photocatalytic H₂ evolution is measured under a 350 W xenon lamp (AHD 350, ShenzhenAnhongda Opto Technology Co. Ltd., China). A 6 ml photoreactor and a cut-off filter ($\lambda > 400$ nm) are used. Photocatalyst powder in which g-C₃N₄ is controlled at 3 mg for the same condition is dispersed in 3 mL aqueous solution with 10 vol% triethanolamine as the hole sacrificial reagent and a magnetic bar to prevent the sedimentation of the photocatalysts during the 6 h measurement. O₂ is removed by the purging of Ar gas before the photocatalytic activity measurements. H₂ evolution is tested by a gas chromatography (SP-3420A, Beifen-Ruili, China) with Ar as carrier gas. H₂ evolution for Pt as cocatalyst was also test in the system. 1%, 2%, 3%, 4% and 5% Pt (H₂PtCl₆, mass ratio to g-C₃N₄) were used. The apparent quantum yield (AQY) which assesses the efficiency of photons conversion is calculated as following^{6,9}:

$$\begin{aligned} \text{AQY}(\%) &= \frac{\text{the number of reacted electrons}}{\text{the number of incident photons}} \times 100\% \\ &= \frac{\text{the number of evolved } H_2 \text{ molecules} \times 2}{\text{the number of incident photons}} \times 100\% \end{aligned}$$

2.5 DFT calculation method

Vienna ab initio simulation package (VASP)^{43, 44} was used in the DFT calculations. Generalized gradient approximation (GGA) in the Perdew - Burke - Ernzerhof (PBE)^{45, 46} form was used in the calculations. A plane wave cutoff energy of 600 eV is sufficient to ensure the convergence of total energies to 1 meV per primitive cell. Supercells were

consisted of $2 \times 2 \times 1$ unit cells and the Brillouin zone was sampled using Monkhorst - Pack mesh $6 \times 6 \times 1$ for them. The forces were converged to $0.01\text{eV}/\text{\AA}$ or below for all structures and the energy accuracy was set at 10^{-6} eV. Van der Waals forces were considered. The vacuum space at least 30\AA was used to avoid the interaction. Because the increase of hydrogen coverage would lead to the decrease of active sites, 25% and 50% monolayer atomic H coverage was considered.

Results and Discussion

3.1 Characterization of structures and morphology

Fig.1A shows the X-ray diffraction (XRD) patterns of raw and composites materials studied herein. The $\text{Ti}_3\text{C}_2\text{T}_x$ is prepared by etching the Al layer of Ti_3AlC_2 powder with HF. -OH, -F and -O surface termination groups spontaneously generate on the surface of Ti_3C_2 during the HF etching process resulting in enhanced hydrophilicity of Ti_3C_2 .^{33, 38} The XRD shifts of the (002) and (004) peaks to lower degrees together with the disappearance of the strongest peak of Ti_3AlC_2 at 39° are the signs of the removal of Al from MAX phase Ti_3AlC_2 .^{10, 40} The XRD pattern of g- C_3N_4 shows a pair of typical peaks with high intensity at $2\theta = 27.5^\circ$ and with low intensity at $2\theta = 13.1^\circ$, as reported previously.³⁴ The XRD patterns of composites samples suggest that the combination of g- C_3N_4 and Ti_3C_2 is through physical contact. No new XRD peak is generated after mixing them in a pestle and mortar and/or followed by annealing in air or N_2 . These strong peaks at $2\theta = 27.5^\circ$ from g- C_3N_4 and at $2\theta = 9^\circ$ from Ti_3C_2 can be both observed in the composites.

Fig.1B shows the FT-IR spectra of these raw and composite materials. No peaks are observed in $\text{Ti}_3\text{C}_2\text{T}_x$ FT-IR spectrum though the C-C and C-Ti bonds are contained. As pure

Ti₃C₂ shows no IR peaks, the IR signals in the composites are obviously from g-C₃N₄. Specifically, the peaks between 3500 and 3000 cm⁻¹ are assigned to the N-H stretching (=NH or -NH₂) and the series peaks near 800 and between 1650 and 1250 cm⁻¹ come from s-triazine derivatives.^{47, 48} The FT-IR spectra of composite samples treated with different annealing conditions are nearly identical to that of pure g-C₃N₄, indicating that g-C₃N₄ and Ti₃C₂ are not chemically bonded.

The morphologies of raw and composites samples were observed by the scanning electronic microscope (SEM) images (Figure 2). The morphology of g-C₃N₄ is bulky, as shown in Figure 2A, whereas the typical 2D nanosheets stacks structure can be clearly observed for the HF etched Ti₃C₂T_x (Figure 2B). When g-C₃N₄ and Ti₃C₂T_x are mixed in a pestle and mortar, the specific morphology characteristics of both g-C₃N₄ and Ti₃C₂T_x still remain, shown Figure 2C, D, E. Although the composites contain more g-C₃N₄ than Ti₃C₂T_x, Ti₃C₂T_x particles are not completely covered by g-C₃N₄ particles. It is noteworthy that annealing of g-C₃N₄/Ti₃C₂T_x composite at 200°C, in N₂ or in air, does not destroy the 2D structure of Ti₃C₂T_x.

Figure 3 shows the X-ray photoelectron spectroscopy (XPS) results of raw and composites materials to study any changes in the surface termination groups of Ti₃C₂ after annealing. The ratio of the peak areas of Ti 2p_{3/2} and Ti 2p_{1/2} is controlled 2 : 1 (Figure 3A). T_x represents the surface termination groups, such as -F, -O and -OH. The peaks at 456 eV and 461 eV are the combinations of the Ti-F bonds, Ti-O bonds and Ti-OH bonds.^{49, 50} The ratio of Ti-T_x bond and Ti-C bond signals varies significantly suggesting the change in the surface termination groups. The Ti-C bond signal remains the same while the Ti-T_x bonds decrease after the

annealing processes are applied. By comparing the peak fitting results of different samples, the increasing signals at 459 eV and 465 eV reflect the decreasing amount of the surface termination groups. The fact that the sample annealed in air exhibits less Ti-T_x bonds than the sample annealed in N₂ can be attributed to the presence of O₂. By comparing the O 1s region spectra, the Ti-O-Ti peak at 530 eV and the Ti-OH peak at 532 eV are separated to identify the -O termination groups (Figure 3B). The proportion of the Ti-O-Ti structure⁵⁰⁻⁵³ as a measure of TiO₂ phase¹⁶ increases after annealing in N₂ and air, though crystalline TiO₂ signal is not detected in the XRD patterns (Figure 1A) g-C₃N₄/Ti₃C₂T_x annealed in air contains the most Ti-O-Ti bonds, g-C₃N₄/Ti₃C₂T_x annealed in N₂ comes second and g-C₃N₄/Ti₃C₂T_x without post treatment contains the least, whereas the proportion of Ti-OH bonds show an opposite ranking.

Table 1 shows the contents of different elements extracted from the XPS spectra to monitor the change of Ti : F ratio upon the annealing methods. The sample annealed in air displays the highest Ti : F ratio confirming the decreasing of the -F terminations after thermal treatment. Previously, Li et al⁴⁰ and Hope et al³⁸ confirmed that the -OH groups on the surface of Ti₃C₂ react as equation (1), when it is heated at 200°C. This reaction mainly takes place during the annealing process resulting in the increasing of Ti-O-Ti groups with the decreasing of Ti-OH.

The presence of O₂ increased the ratio of Ti-O-Ti during annealing, according to the higher Ti-O-Ti content when annealed in air. Meanwhile, the content of -F terminations decreased for both annealing processes regardless of the atmosphere, N₂ or air, at a relatively low temperature (200°C). However, the mechanism corresponding to -F removal was still

unclear. The samples annealed in air demonstrate the least -F ratio and the most Ti-O-Ti ratio comparing the parallel samples, though the exact ratio of Ti-O-Ti, Ti-OH, and Ti-F cannot be identified by the XPS spectra.

The morphology of g-C₃N₄ with 30% Ti₃C₂ annealed in air is assessed via HRTEM in Figure S1. Low magnification image demonstrates the hybrid of g-C₃N₄ and Ti₃C₂. The layered structure of g-C₃N₄ is clearly shown. The high magnification image displays the interface of the hybrid. As g-C₃N₄ and Ti₃C₂ layers can be observed obviously, the heterojunction interface is considered formed.

3.2 UV-Vis DRS characterization

Figure 4 displays the UV-vis diffuse reflectance spectra (UV-vis DRS) of raw and composites materials; UV-vis DRS is a widely adopted method in investigating the optical absorption in semiconductor-based photo-catalysis. The fact that the Ti₃C₂T_x exhibits no obvious absorption edge is attributed to its metallic nature.³³ On the other hand, the pure g-C₃N₄ and the g-C₃N₄/Ti₃C₂ composites exhibit an absorption band around the wavelength of 460 nm reflecting the bandgap of g-C₃N₄, and this bandgap is insensitive to the annealing process.⁵⁴ The presence of the black Ti₃C₂T_x merely increases the absorption baseline in the composites as reported previously.³³ Though the absorption edges changed slightly, no obvious red shift or shoulder absorption are observed. Thus the band gaps of the composites do not change. In view of this, light absorption is a negligible factor in discussing the resulting HER performance by these g-C₃N₄/Ti₃C₂ composites.

3.3 Photocatalytic performance of g-C₃N₄/Ti₃C₂ composites

These composite materials were then tested in photocatalysis for water splitting. Figure 6A compares HER results using g-C₃N₄/Ti₃C₂ composites in which Ti₃C₂ functions as co-catalysis. The photo-catalytic H₂ productions by the g-C₃N₄/Ti₃C₂ composites are evaluated with visible light irradiation ($\lambda > 400$ nm). The maximum H₂ production rate of the composite material without annealing is merely 5.3 $\mu\text{mol/h/g.cat}$ after optimization the ratio of Ti₃C₂ in the composite to 30%. After annealing this composite at 200°C in N₂, the H₂ production increased to 7.8 $\mu\text{mol/h/g.cat}$, which is 45.2% higher than without annealing at the same ratio of g-C₃N₄ to Ti₃C₂. Moreover, the H₂ production of g-C₃N₄ with 30% Ti₃C₂ after annealing in air can achieve 10.9 $\mu\text{mol/h/g.cat}$, which is further 41.06% higher than that of the sample annealed in N₂ and 104.84% higher than without annealing. However, the best HER performance is achieved at different mass ratios for these composites samples (Figure S2). The best performance for g-C₃N₄/Ti₃C₂ composites annealed in N₂ is achieved at a ratio of 70%, with an HER reaching 14.2 $\mu\text{mol/h/g.cat}$, which is 166% higher than the best performance of non-annealed composite. Importantly, the HER performance of the composite of g-C₃N₄ with 190% Ti₃C₂ annealed in air gives the best performance among all, with a H₂ production as high as 88 $\mu\text{mol/h/g.cat}$, which is a 15-fold increasing compared the best non-annealed composite, compared with 53.3 $\mu\text{mol/h/g.cat}$ using Co₂P as cocatalyst.⁷ Meanwhile, the highest AQY achieves 1.27%, the same order of magnitude as reported.⁶ What is more, the Pt cocatalyst is also compared in the system (Figure S3), g-C₃N₄ with 3% Pt demonstrates the best performance for 56.2 $\mu\text{mol/h/g.cat}$, which is lower than that of g-C₃N₄ with 190% Ti₃C₂ annealed in air. The stability of the hybrid is also considered, there is a 64% decrease of hydrogen evolution rate for g-C₃N₄ with 30% Ti₃C₂ annealed in air after

4 cycles and 24 h of tests. This is mainly caused by the separation of g-C₃N₄ and Ti₃C₂. The heterojunction interface disappears though the XRD spectra (Figure S4) show no obvious differences before and after the photocatalytic activity tests.

Figure 6B shows the photoluminescence (PL) spectra of the samples used in HER measurements. These PL spectra exhibit an identical emission peak at 463 nm. The bare g-C₃N₄ shows the strongest PL signal due to the spontaneous recombination of the photogenerated electron-hole pairs. The composites of Ti₃C₂/g-C₃N₄ containing 30% Ti₃C₂ exhibit reduced PL intensity owing to the prevention of recombination of the photogenerated electron-hole pairs by Ti₃C₂, which is one of the reasons of enhanced HER activity.

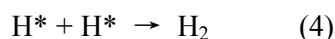
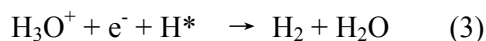
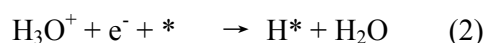
Table 2 lists the specific surface area obtained from the BET measurements of the g-C₃N₄ with 30% Ti₃C₂ samples. The surface area of these samples are coincident with their HER performance. Specifically, the annealed samples have higher specific surface area than without annealing, and the performances of photocatalysis activity of the formers are also better than that of the latter. The higher specific surface area provides more active sites for the HER reactions including the depleting of the photogenerated holes by the triethanolamine on the surface of g-C₃N₄ and/or the H₂ production on the surface of Ti₃C₂T_x.

3.4 Photocatalytic and HER mechanism

The photocatalyst g-C₃N₄ is excited by the white light and then electron-hole pairs are generated. The electrons gather on Ti₃C₂ through the ohmic contact between g-C₃N₄ with the semiconductor nature and the metallic MXenes, resulting in a negative shift of the Fermi level,^{33, 34} and this will improve the separation of the electron-hole pairs. The holes left on the semiconductor are reduced by the electron donor or electron scavenger, triethanolamine. As

shown in Table 1, the increasing specific surface area provides more active sites to sacrifice the holes and separates the electron-hole pairs as well.

We consider the reaction mechanism of the HER on the surface of the MXenes is the same as the one in electrocatalysis because of the same active sites and electron with high energy. Thus, the H₂ production react as the following Equation(2), (3) and (4) as the three main steps as reported:^{55, 56}



The * represent the active sites for the HER and are considered to be the -O surface termination groups on the surface of Ti₃C₂ here.^{33, 57} Thus H₃O⁺ ion can be adsorbed on the -O surface terminations and combine with an electron to form an H atom, which is known as the Volmer reaction. At the same active site, H atom combines another H₃O⁺ ion from water and an electron from Ti₃C₂ to form a H₂ molecule as in equation (2), which is called the Heyrovsky mechanism. Two H atoms on the active sites form a H₂ molecule which is considered the Tafel mechanism in equation (3). Hydrogen molecules form with the presence of photogenerated electrons and H₃O⁺ ions at the active sites, the -O surface terminations. Therefore more -O surface terminations improve the HER performance and the g-C₃N₄/Ti₃C₂ composite annealed in the air exhibits the best photocatalytic activity.

3.5 DFT calculations

Figure 7A showed the top and side views of the Ti₃C₂ structure. a, b and c represent the space sites for termination groups on the surface of Ti₃C₂. a were on top of C atoms, b were

over the surface Ti atoms and c were over the mid-layered Ti atoms. The -O and -F terminations occupied the c sites and -OH termination groups were not considered because of is indirectly connected to the primary step in HER mechanism.⁵⁸ Figure 7B, C and D demonstrated the Gibbs free energies (ΔG_{H}) of bare, -O and -F terminated Ti_3C_2 with the atomic H coverage of 25% and 50%, respectively. The near-zero $|\Delta G_{\text{H}}|$ which mean the high HER catalytic ability was desirable. $|\Delta G_{\text{H}}|$ of all structures were exhibited in Table S1 in details. -F terminated Ti_3C_2 demonstrated a high $|\Delta G_{\text{H}}|$ value and the best structure for HER co-catalyst was Ti_3C_2 with -O terminations, of which the $|\Delta G_{\text{H}}|$ was as low as 0.01 eV. $|\Delta G_{\text{H}}|$ of typical HER co-catalyst Pt(111) was 0.09 eV and MoS_2 was 0.08 eV,^{59, 60} both were much higher than that of Ti_3C_2 with -O terminations. Thus -O terminated Ti_3C_2 was a better replacement of noble metal Pt as the co-catalyst for HER. The $|\Delta G_{\text{H}}|$ of 25% atomic H covered Ti_3C_2 with -O terminations was much lower than that of 50% atomic H covered Ti_3C_2 . This was mainly caused by the decrease of the active site for HER, thus 25% atomic H coverage of Ti_3C_2 with -O terminations showed the best catalytic ability for HER.

Conclusions

In summary, the two-dimensional titanium carbide MXene Ti_3C_2 is investigated as a co-catalyst for its HER activity by variation of the mixed ratio of g- C_3N_4 with Ti_3C_2 and by modifying the surface termination groups on the surface of Ti_3C_2 . The best HER performance is obtained at the g- $\text{C}_3\text{N}_4/\text{Ti}_3\text{C}_2$ ratio of 190% followed by annealing in air in muffle furnace with a high H_2 production of 88 $\mu\text{mol/h/g.cat}$. The AQY achieves as high as 1.27%. The increased HER is attributed to the higher specific surface area providing more active sites and the -O surface terminations of Ti_3C_2 , which improved the separation of the electron-hole pairs.

Our findings illustrate that Ti_3C_2 MXene can be used as co-catalyst in g- C_3N_4 -based photocatalytic HER, thus paving the way for the commercialization of MXenes for solar energy conversion. The DFT calculations showed that the Ti_3C_2 with -O surface terminations and 25% covered H atoms demonstrated the lowest free energy at 0.011eV, and also confirmed the experimental result that Ti_3C_2 with -O surface termination shows the best HER activity as co-catalyst in photocatalysis.

Conflict of interest

There are no conflicts to declare.

Acknowledgements

This work is supported by the Natural Science Foundation of China (No. 11574111 to X-F.W.), Natural Science Foundation of Jilin Province (No. 20160101303JC to X-F.W.). Acknowledgements to Prof. Yury Gogotsi and the Thousand Talents Program (China).

References

1. H. Yu, P. Xiao, P. Wang and J. Yu, *Applied Catalysis B: Environmental*, 2016, **193**, 217-225.
2. H. Pan, Y.-W. Zhang, V. B. Shenoy and H. Gao, *ACS Catalysis*, 2011, **1**, 99-104.
3. X. Wang, K. Maeda, A. Thomas, K. Takanabe, G. Xin, J. M. Carlsson, K. Domen and M. Antonietti, *Nature materials*, 2009, **8**, 76-80.
4. W. J. Ong, L. L. Tan, Y. H. Ng, S. T. Yong and S. P. Chai, *Chemical reviews*, 2016, **116**, 7159-7329.
5. W.-J. Ong, *Frontiers in Materials*, 2017, **4**, 11.
6. D. Zeng, W.-J. Ong, H. Zheng, M. Wu, Y. Chen, D.-L. Peng and M.-Y. Han, *Journal of Materials Chemistry A*, 2017, **5**, 16171-16178.
7. D. Zeng, W.-J. Ong, Y. Chen, S. Y. Tee, C. S. Chua, D.-L. Peng and M.-Y. Han, *Particle & Particle Systems Characterization*, 2018, **35**, 1700251.
8. D. Zeng, P. Wu, W.-J. Ong, B. Tang, M. Wu, H. Zheng, Y. Chen and D.-L. Peng, *Applied Catalysis B: Environmental*, 2018, **233**, 26-34.
9. D. Zeng, W. Xu, W.-J. Ong, J. Xu, H. Ren, Y. Chen, H. Zheng and D.-L. Peng, *Applied Catalysis B: Environmental*, 2018, **221**, 47-55.
10. M. Naguib, M. Kurtoglu, V. Presser, J. Lu, J. Niu, M. Heon, L. Hultman, Y. Gogotsi and M. W. Barsoum, *Advanced materials*, 2011, **23**, 4248-4253.
11. M. Naguib, V. N. Mochalin, M. W. Barsoum and Y. Gogotsi, *Advanced materials*, 2014, **26**, 992-1005.
12. B. Anasori, M. R. Lukatskaya and Y. Gogotsi, *Nature Reviews Materials*, 2017, **2**, 16098.
13. Y. Dall'Agnese, P. L. Taberna, Y. Gogotsi and P. Simon, *The journal of physical chemistry letters*, 2015, **6**, 2305-2309.
14. C. J. Zhang, B. Anasori, A. Seral-Ascaso, S. H. Park, N. McEvoy, A. Shmeliov, G. S. Duesberg, J. N. Coleman, Y. Gogotsi and V. Nicolosi, *Advanced materials*, 2017, **29**.
15. M.-Q. Zhao, M. Torelli, C. E. Ren, M. Ghidui, Z. Ling, B. Anasori, M. W. Barsoum and Y. Gogotsi, *Nano Energy*, 2016, **30**, 603-613.
16. M. Naguib, J. Come, B. Dyatkin, V. Presser, P.-L. Taberna, P. Simon, M. W. Barsoum and Y. Gogotsi, *Electrochemistry Communications*, 2012, **16**, 61-64.
17. M. Q. Zhao, X. Xie, C. E. Ren, T. Makaryan, B. Anasori, G. Wang and Y. Gogotsi, *Advanced materials*, 2017, **29**.
18. S.-Y. Lin and X. Zhang, *Journal of Power Sources*, 2015, **294**, 354-359.
19. L. Li, M. Zhang, X. Zhang and Z. Zhang, *Journal of Power Sources*, 2017, **364**, 234-241.
20. Q. Fu, J. Wen, N. Zhang, L. Wu, M. Zhang, S. Lin, H. Gao and X. Zhang, *RSC Advances*, 2017, **7**, 11998-12005.
21. F. Shahzad, M. Alhabeab, C. B. Hatter, B. Anasori, H. S. Man, C. M. Koo and Y. Gogotsi, *Science*, 2016, **353**, 1137.
22. X. Li, X. Yin, M. Han, C. Song, H. Xu, Z. Hou, L. Zhang and L. Cheng, *Journal of Materials Chemistry C*, 2017, **5**, 4068-4074.

23. M. Han, X. Yin, H. Wu, Z. Hou, C. Song, X. Li, L. Zhang and L. Cheng, *ACS applied materials & interfaces*, 2016, **8**, 21011-21019.
24. M. Ming, Y. Ren, M. Hu, Y. Zhang, T. Sun, Y. Ma, X. Li, W. Jiang, D. Gao, J. Bi and G. Fan, *Applied Catalysis B: Environmental*, 2017, **210**, 462-469.
25. Y. Ying, Y. Liu, X. Wang, Y. Mao, W. Cao, P. Hu and X. Peng, *ACS applied materials & interfaces*, 2015, **7**, 1795-1803.
26. Q. Peng, J. Guo, Q. Zhang, J. Xiang, B. Liu, A. Zhou, R. Liu and Y. Tian, *Journal of the American Chemical Society*, 2014, **136**, 4113-4116.
27. Z. W. Seh, K. D. Fredrickson, B. Anasori, J. Kibsgaard, A. L. Strickler, M. R. Lukatskaya, Y. Gogotsi, T. F. Jaramillo and A. Vojvodic, *ACS Energy Letters*, 2016, **1**, 589-594.
28. M. Khazaei, M. Arai, T. Sasaki, C.-Y. Chung, N. S. Venkataramanan, M. Estili, Y. Sakka and Y. Kawazoe, *Advanced Functional Materials*, 2013, **23**, 2185-2192.
29. Y. Xie and P. Kent, *Physical Review B*, 2013, **87**, 235441.
30. Y. Gao, L. Wang, A. Zhou, Z. Li, J. Chen, H. Bala, Q. Hu and X. Cao, *Materials Letters*, 2015, **150**, 62-64.
31. C. Peng, X. Yang, Y. Li, H. Yu, H. Wang and F. Peng, *ACS applied materials & interfaces*, 2016, **8**, 6051-6060.
32. H. Wang, R. Peng, Z. D. Hood, M. Naguib, S. P. Adhikari and Z. Wu, *ChemSusChem*, 2016, **9**, 1490-1497.
33. J. Ran, G. Gao, F. T. Li, T. Y. Ma, A. Du and S. Z. Qiao, *Nature communications*, 2017, **8**, 13907.
34. M. Shao, Y. Shao, J. Chai, Y. Qu, M. Yang, Z. Wang, M. Yang, W. F. Ip, C. T. Kwok, X. Shi, Z. Lu, S. Wang, X. Wang and H. Pan, *Journal of Materials Chemistry A*, 2017, **5**, 16748-16756.
35. T. Su, R. Peng, Z. D. Hood, M. Naguib, I. N. Ivanov, J. K. Keum, Z. Qin, Z. Guo and Z. Wu, *ChemSusChem*, 2018, **11**, 688-699.
36. .
37. N. Li, X. Chen, W. J. Ong, D. R. MacFarlane, X. Zhao, A. K. Cheetham and C. Sun, *ACS Nano*, 2017, **11**, 10825-10833.
38. M. A. Hope, A. C. Forse, K. J. Griffith, M. R. Lukatskaya, M. Ghidui, Y. Gogotsi and C. P. Grey, *Physical chemistry chemical physics : PCCP*, 2016, **18**, 5099-5102.
39. Y. Xie, M. Naguib, V. N. Mochalin, M. W. Barsoum, Y. Gogotsi, X. Yu, K. W. Nam, X. Q. Yang, A. I. Kolesnikov and P. R. Kent, *Journal of the American Chemical Society*, 2014, **136**, 6385-6394.
40. Z. Li, L. Wang, D. Sun, Y. Zhang, B. Liu, Q. Hu and A. Zhou, *Materials Science and Engineering: B*, 2015, **191**, 33-40.
41. M. Naguib, O. Mashtalir, M. R. Lukatskaya, B. Dyatkin, C. Zhang, V. Presser, Y. Gogotsi and M. W. Barsoum, *Chemical communications*, 2014, **50**, 7420-7423.
42. X. Lu, K. Xu, P. Chen, K. Jia, S. Liu and C. Wu, *J. Mater. Chem. A*, 2014, **2**, 18924-18928.
43. G. Kresse and J. Furthmüller, *Physical Review B Condensed Matter*, 1996, **54**, 11169.
44. G. Kresse and D. Joubert, *Physical Review B*, 1999, **59**, 1758.

45. J. P. Perdew, J. A. Chevary, S. H. Vosko, K. A. Jackson, M. R. Pederson, D. J. Singh and C. Fiolhais, *Physical Review B Condensed Matter*, 1992, **46**, 6671.
46. J. P. Perdew and Y. Wang, *Physical Review B Condensed Matter*, 1992, **45**, 13244.
47. Y. Li, J. Zhang, Q. Wang, Y. Jin, D. Huang, Q. Cui and G. Zou, *The Journal of Physical Chemistry B*, 2010, **114**, 9429-9434.
48. B. V. Lotsch, M. Doblinger, J. Sehnert, L. Seyfarth, J. Senker, O. Oeckler and W. Schnick, *Chemistry*, 2007, **13**, 4969-4980.
49. C. E. Ren, M.-Q. Zhao, T. Makaryan, J. Halim, M. Boota, S. Kota, B. Anasori, M. W. Barsoum and Y. Gogotsi, *ChemElectroChem*, 2016, **3**, 689-693.
50. A. Lipatov, M. Alhabeab, M. R. Lukatskaya, A. Boson, Y. Gogotsi and A. Sinitskii, *Advanced Electronic Materials*, 2016, **2**, 1600255.
51. B. Ahmed, D. H. Anjum, M. N. Hedhili, Y. Gogotsi and H. N. Alshareef, *Nanoscale*, 2016, **8**, 7580-7587.
52. O. Mashtalir, K. M. Cook, V. N. Mochalin, M. Crowe, M. W. Barsoum and Y. Gogotsi, *J. Mater. Chem. A*, 2014, **2**, 14334-14338.
53. T. Zhang, L. Pan, H. Tang, F. Du, Y. Guo, T. Qiu and J. Yang, *Journal of Alloys and Compounds*, 2017, **695**, 818-826.
54. Y. Kang, Y. Yang, L. C. Yin, X. Kang, G. Liu and H. M. Cheng, *Advanced materials*, 2015, **27**, 4572-4577.
55. J. Deng, P. Ren, D. Deng, L. Yu, F. Yang and X. Bao, *Energy Environ. Sci.*, 2014, **7**, 1919-1923.
56. B. Conway and B. Tilak, *Electrochimica Acta*, 2002, **47**, 3571-3594.
57. C. Ling, L. Shi, Y. Ouyang, Q. Chen and J. Wang, *Advanced science*, 2016, **3**, 1600180.
58. M. Pandey and K. S. Thygesen, *The Journal of Physical Chemistry C*, 2017, **121**, 13593-13598.
59. J. K. Nørskov, T. Bligaard, A. Logadottir, J. R. Kitchin, J. G. Chen, S. Pandelov and U. Stimming, *Journal of The Electrochemical Society*, 2005, **152**, J23.
60. J. Bonde, P. G. Moses, T. F. Jaramillo, J. K. Nørskov and I. Chorkendorff, *Faraday discussions*, 2009, **140**, 219-231.

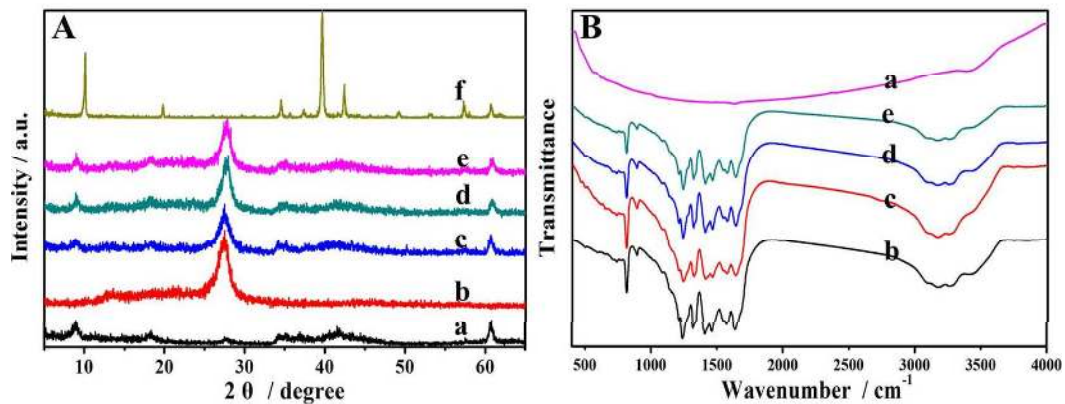


Figure 1. A) The XRD patterns of the two pure materials and the hybrids B) The FTIR spectra of the two pure materials and the composites. a) Ti_3C_2 , b) $\text{g-C}_3\text{N}_4$, c) $\text{g-C}_3\text{N}_4$ with 30% Ti_3C_2 , d) $\text{g-C}_3\text{N}_4$ with 30% Ti_3C_2 annealed in N_2 , e) $\text{g-C}_3\text{N}_4$ with 30% Ti_3C_2 annealed in air and f) Ti_3AlC_2 .

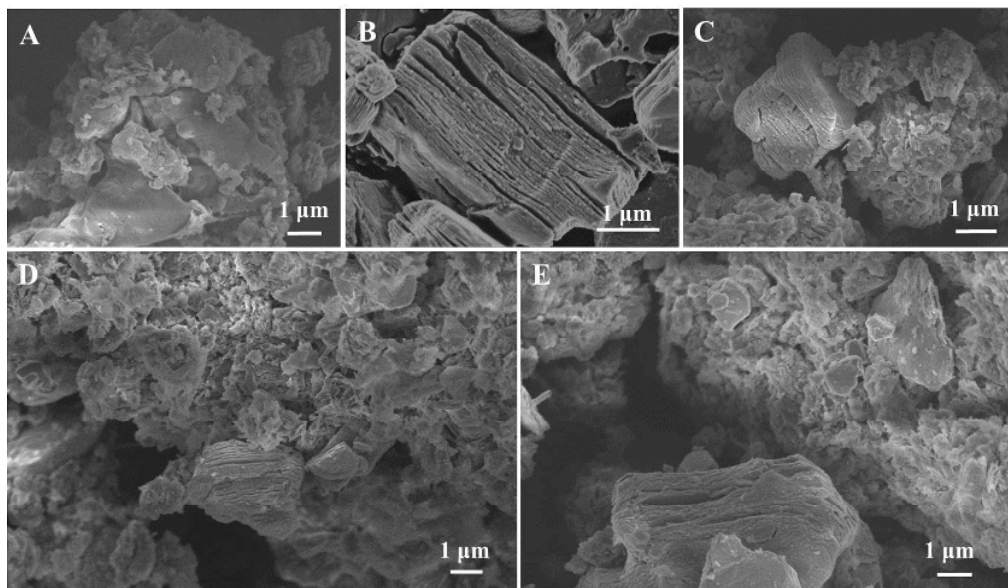


Figure 2. The SEM image of A) g-C₃N₄ B) Ti₃C₂ C) g-C₃N₄ with 30% Ti₃C₂ D) g-C₃N₄ with 30% Ti₃C₂ annealed in N₂ E) g-C₃N₄ with 30% Ti₃C₂ annealed in air.

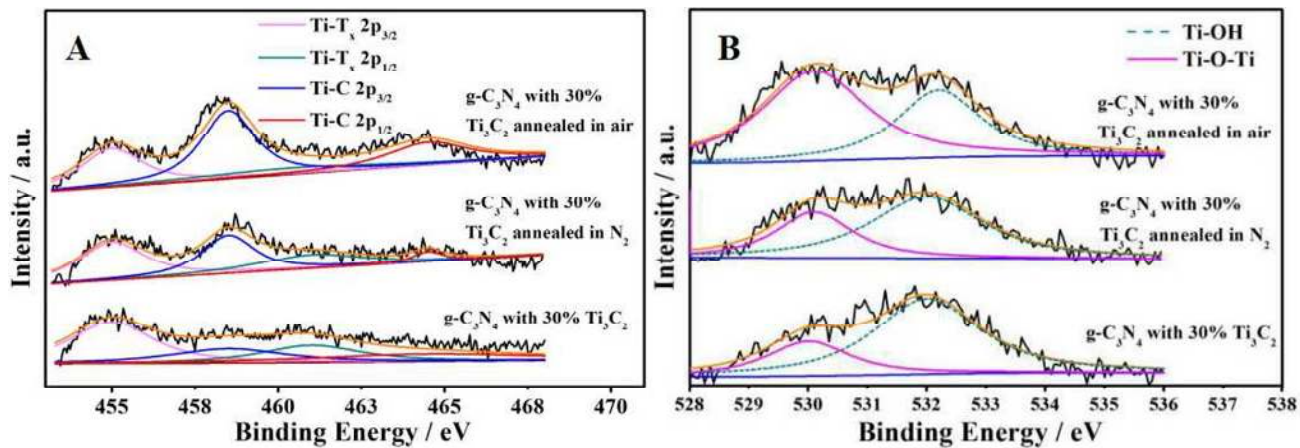


Figure 3. The XPS spectra of O 1s region (A) and Ti 2p region (B) for g-C₃N₄ with 30% Ti₃C₂, g-C₃N₄ with 30% Ti₃C₂ annealed in N₂ and g-C₃N₄ with 30% Ti₃C₂ annealed in air.

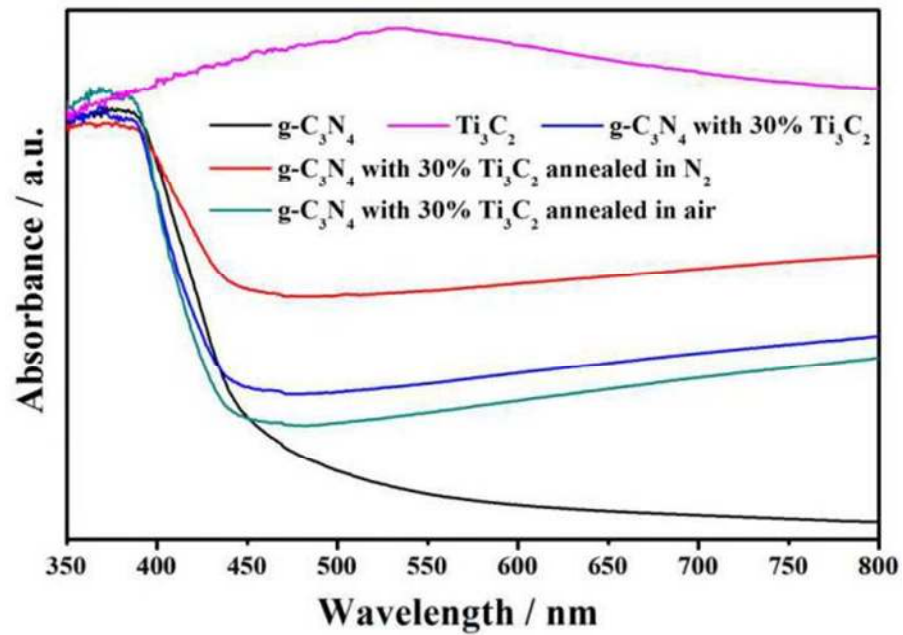


Figure 4. The DRS spectra of $g-C_3N_4$, Ti_3C_2 , $g-C_3N_4$ with 30% Ti_3C_2 , $g-C_3N_4$ with 30% Ti_3C_2 annealed in N_2 and $g-C_3N_4$ with 30% Ti_3C_2 annealed in air.

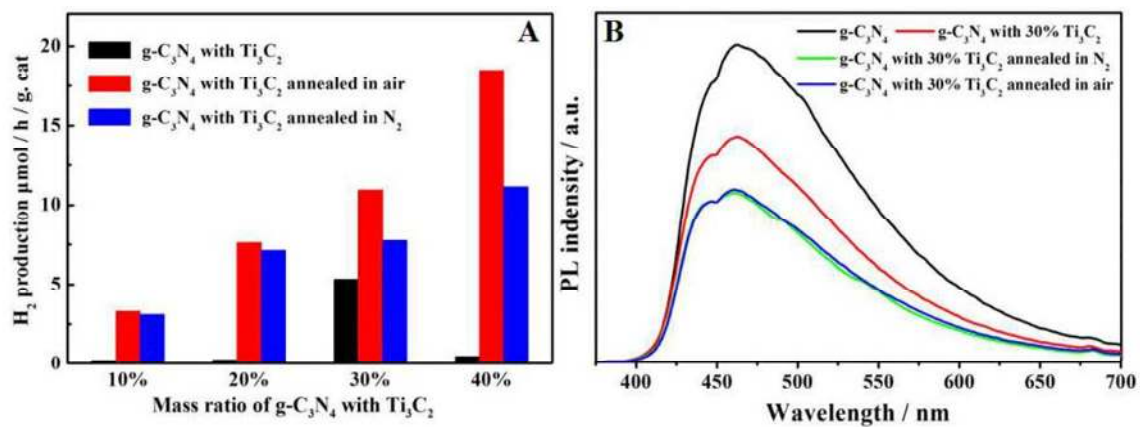


Figure 5. A) The production of g-C₃N₄, g-C₃N₄ with Ti₃C₂, g-C₃N₄ with Ti₃C₂ annealed in N₂ and g-C₃N₄ with Ti₃C₂ annealed in air at different ratios B) The PL spectra at an excitation wavelength of 340 nm.

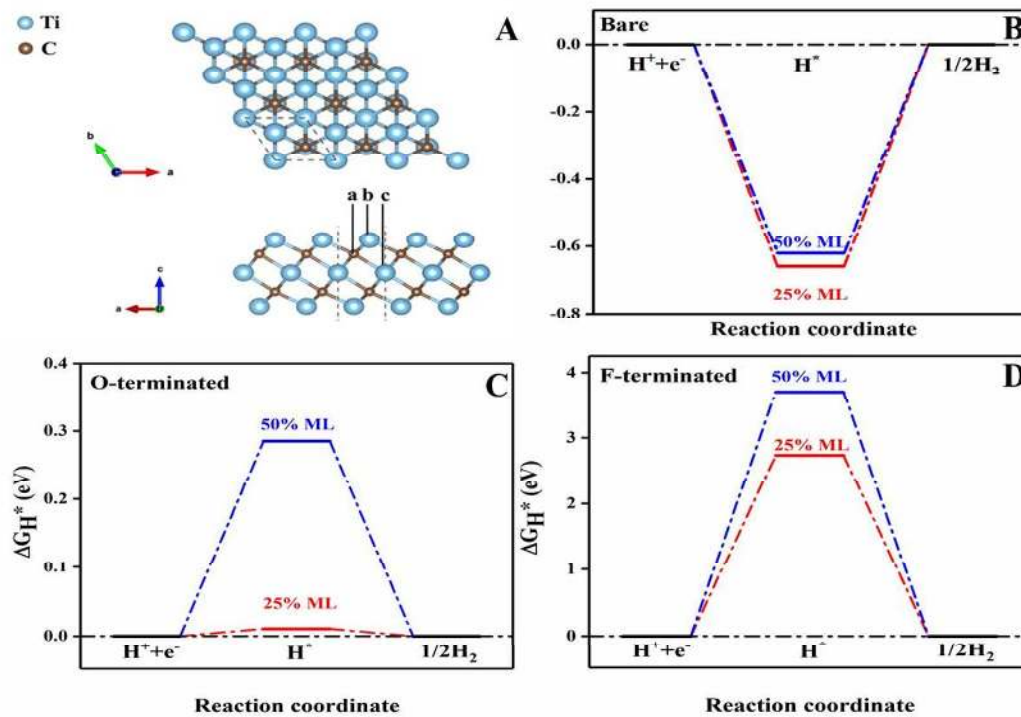


Figure 6. A) The top view and side view of Ti_3C_2 , free energy of B) bare, C) -O terminated and D) -F terminated Ti_3C_2 with 25% and 50% coverages of atomic H.

Table 1. The XPS surveys of A) g - C₃N₄ B) g-C₃N₄ with 30% Ti₃C₂, C) g-C₃N₄ with 30% Ti₃C₂ annealed in N₂ and D) g-C₃N₄ with 30% Ti₃C₂ annealed in air.

Samples	C	N	O	F	Ti
g-C ₃ N ₄	55.7	41	3.3		
g-C ₃ N ₄ with 30% Ti ₃ C ₂	54.3	36.5	5.9	2.1	1.2
g-C ₃ N ₄ with 30% Ti ₃ C ₂ annealed in N ₂	56.2	36.2	4.6	1.5	1.5
g-C ₃ N ₄ with 30% Ti ₃ C ₂ annealed in air	53.9	37.3	5.7	1.2	1.8

Table 2. The specific surface area for different samples.

Samples	BET m²/g
g-C ₃ N ₄	55
Ti ₃ C ₂	6
g-C ₃ N ₄ with 30% Ti ₃ C ₂	36
g-C ₃ N ₄ with 30% Ti ₃ C ₂ annealed in N ₂	50
g-C ₃ N ₄ with 30% Ti ₃ C ₂ annealed in air	49